

# Population III star formation in a $\Lambda$ CDM universe, II: Effects of a photodissociating background

Brian W. O'Shea<sup>1</sup> & Michael L. Norman<sup>2</sup>

## ABSTRACT

We examine aspects of primordial star formation in the presence of a molecular hydrogen-dissociating ultraviolet background. We compare a set of AMR hydrodynamic cosmological simulations using a single cosmological realization but with a range of ultraviolet background strengths in the Lyman-Werner band. This allows us to study the effects of Lyman-Werner radiation on suppressing  $\text{H}_2$  cooling at low densities as well as the high-density evolution of the collapsing cloud core in a self-consistent cosmological framework. We find that the addition of a photodissociating background results in a delay of the collapse of high density gas at the center of the most massive halo in the simulation and, as a result, an increase in the virial mass of this halo at the onset of baryon collapse. We find that, contrary to previous results, Population III star formation is not suppressed for  $J_{21} \geq 0.1$ , but occurs even with backgrounds as high as  $J_{21} = 1$ . We find that  $\text{H}_2$  cooling leads to collapse despite the depressed core molecular hydrogen fractions due to the elevated  $\text{H}_2$  cooling rates at  $T = 2 - 5 \times 10^3$  K. We observe a relationship between the strength of the photodissociating background and the rate of accretion onto the evolving protostellar cloud core, with higher LW background fluxes resulting in higher accretion rates. Finally, we find that the collapsing cloud cores in our simulations do not fragment at densities below  $n \sim 10^{10} \text{ cm}^{-3}$  regardless of the strength of the LW background, suggesting that Population III stars forming in halos with  $T_{\text{vir}} \sim 10^4$  K may still form in isolation.

*Subject headings:* cosmology: theory — galaxies: high-redshift — stars: formation — hydrodynamics

---

<sup>1</sup>Theoretical Astrophysics (T-6), MS B227, Los Alamos National Laboratory, Los Alamos, NM 87545; bwoshea@lanl.gov

<sup>2</sup>Center for Astrophysics and Space Sciences, University of California at San Diego, La Jolla, CA 92093; mlnorman@ucsd.edu

## 1. Introduction

The study of the formation of Population III stars in a cosmological context via high-resolution simulations is becoming a mature discipline, with multiple groups finding similar results (Bromm, Coppi, & Larson 2002; Bromm & Loeb 2004; Abel, Bryan, & Norman 2002; O’Shea & Norman 2007; Yoshida et al. 2006b; Gao et al. 2006). However, all of these calculations operate under a common fundamental assumption – namely, the absence of an ultraviolet background. Given the abundance of halos in which Population III stars would form and the general consensus that these stars must be massive, one expects that, though only a small fraction of the volume of the universe would be ionized, a significant background of ultraviolet radiation in the Lyman-Werner (LW) band (11.18-13.6 eV), which is capable of photodissociating molecular hydrogen, would be present for the formation of the bulk of Population III stars (Omukai 2001; Yoshida et al. 2003; Machacek, Bryan, & Abel 2001; Wise & Abel 2005). Given that atomic hydrogen is optically thin to this radiation and that it easily destroys molecular hydrogen, this could have a significant impact on the formation of primordial stars. Machacek et al. (2001) used cosmological AMR simulations to study the formation of primordial stars in the presence of a soft UV background, and later including an x-ray background (Machacek, Bryan, & Abel 2003). They found that the LW background delays the formation of Population III stars and shifts halo formation to higher masses. However, their calculations were not of sufficiently high resolution to give any significant information about the formation of the protostellar cloud at the core of each collapsing cosmological halo. Yoshida et al. (2003) performed a suite of large SPH simulations of high redshift structure formation, including two calculations with a soft UV background with  $J_{21} = 0.01$  and  $0.1$ , where  $J_{21}$  is the mean intensity of the UV background in the LW band in units of  $10^{-21}$  erg s $^{-1}$  cm $^{-2}$  Hz $^{-1}$  sr $^{-1}$ . They found that gas cooling is suppressed in the higher LW background case, and predicted that star formation would not occur. On the other hand, Oh & Haiman (2002) showed analytically that primordial gas in halos with  $T_{vir} \gtrsim 10^4$  K can still collapse to high densities in the presence of a strong molecular hydrogen-dissociating background via atomic hydrogen line radiation, and can eventually form H $_2$ . They referred to these objects as “second generation objects” in the sense that although still of primordial composition, their formation pathway is different from the first stars.

An issue that needs to be addressed concerns the mode of primordial star formation in halos with  $T_{vir} \sim 10^4$  K and above. It is apparent from recent studies using large numbers of simulations that smaller halos, with masses of  $\sim 10^5 - 10^6$  M $_{\odot}$ , appear to always form primordial stars in isolation (Gao et al. 2006; O’Shea & Norman 2007). Is this still the case in halos whose masses are an order of magnitude or more larger? Does a single primordial star form, or several? This is particularly relevant given that many semi-

analytic models of structure formation that follow the chemical evolution of structures at high redshift (Scannapieco et al. 2005; Schneider et al. 2006) suggest that halos of this scale which have not been enriched by metals (and thus will form primordial stars) exist up to at least  $z \sim 5$ . If this is true, there is expected to be a strong photodissociating background at that time (Yoshida et al. 2003; Wise & Abel 2005).

This paper is the second in a series. In O’Shea & Norman (2007) (hereafter referred to as Paper I), we examined several aspects of Population III star formation in a  $\Lambda$ CDM universe, in the absence of an ultraviolet background which photodissociates molecular hydrogen. In this paper, we study Population III star formation in a single cosmological realization varying the strength of the LW background, with the goal of investigating the effect that this background has on the evolution and properties of gas in the halo core (at radii  $\ll 1$  pc) and the ultimate fate of the gas at the center of  $T_{vir} \sim 10^4$  K halos. We use a single cosmological realization, varying the strength of the photodissociating background over the range suggested by Wise & Abel (2005), and look for the cutoff in Population III star formation suggested by Yoshida et al. (2003).

In agreement with the findings of (Machacek et al. 2001), we find that the addition of a photodissociating background results in a delay of the collapse of high density gas at the center of the most massive halo in the simulation and, as a result, an increase in the virial mass of this halo at the onset of baryon collapse. We find that, contrary to the results of Yoshida et al. (2003), star formation is not suppressed for  $J_{21} \geq 0.1$ , but occurs even with backgrounds as high as  $J_{21} = 1$ . We find that  $H_2$  cooling leads to collapse despite the depressed halo core molecular hydrogen fractions  $f_{H_2} \sim 10^{-6}$  by two multiplicative effects: (1) the elevated  $H_2$  cooling rates per molecule at  $T = 2 - 5 \times 10^3$  K, and (2) time. We find that halo core collapse occurs in the usual way once the gas in the halo core has become dense enough that the cooling time becomes much less than the Hubble time. We also observe a relationship between the strength of the photodissociating background and the rate of accretion onto the evolving protostellar cloud core, with higher LW background fluxes resulting in higher accretion rates. This is a simple consequence of the suppression of molecular hydrogen formation (and thus suppression of cooling) by the photodissociating background, as well as the higher virial temperatures of the more massive halos at the epoch of collapse. This may have implications for the range of Population III stellar masses. Finally, we find that the collapsing halo cores in our simulations do not fragment at densities below  $n \sim 10^{10} \text{ cm}^{-3}$  regardless of the strength of the soft UV background, suggesting that Population III stars forming in halos with  $T_{vir} \sim 10^4$  K may still form in isolation.

The organization of this paper is as follows. In Section 2 we provide a description of Enzo, the code used to perform the calculations in this paper and of the simulation

setup. The results from our simulations are presented in Sections 3 through 7: Section 3 discusses some of the mean halo properties observed in the calculations, Section 4 discusses the evolution of the halo core prior to collapse, Section 5 compares spherically-averaged halo properties for all simulations at the epoch of collapse, Section 6 discusses a variety of halo properties at a fixed redshift, and Section 7 compares the evolution of two representative simulations taken from our ensemble. In Section 8 we discuss neglected physics and possible numerical issues, and in Section 9 we discuss some of the results presented in this work and their implications. Finally, we present a summary of the main results in Section 10.

## 2. Methodology

### 2.1. The Enzo code

‘Enzo’<sup>1</sup> is a publicly available, extensively tested adaptive mesh refinement (AMR) cosmology code developed by Greg Bryan and others (Bryan & Norman 1997a, 1997b; Norman & Bryan 1999; O’Shea et al. 2004, 2005b). The specifics of the Enzo code are described in detail in these papers (and references therein), but we present a brief description here for clarity.

The Enzo code couples an N-body particle-mesh (PM) solver (Efsthathiou et al. 1985; Hockney & Eastwood 1988) used to follow the evolution of a collisionless dark matter component with an Eulerian AMR method for ideal gas dynamics by Berger & Colella (1989), which allows high dynamic range in gravitational physics and hydrodynamics in an expanding universe. This AMR method (referred to as *structured* AMR) utilizes an adaptive hierarchy of grid patches at varying levels of resolution. Each rectangular grid patch (referred to as a “grid”) covers some region of space in its *parent grid* which requires higher resolution, and can itself become the parent grid to an even more highly resolved *child grid*. Enzo’s implementation of structured AMR places no fundamental restrictions on the number of grids at a given level of refinement, or on the number of levels of refinement. However, owing to limited computational resources it is practical to institute a maximum level of refinement,  $\ell_{max}$ . Additionally, the Enzo AMR implementation allows arbitrary integer ratios of parent and child grid resolution, though in general for cosmological simulations (including the work described in this paper) a refinement ratio of 2 is used.

Since the addition of more highly refined grids is adaptive, the conditions for refinement must be specified. In Enzo, the criteria for refinement can be set by the user to be a combi-

---

<sup>1</sup><http://lca.ucsd.edu/portal/software/enzo/>

nation of any or all of the following: baryon or dark matter overdensity threshold, minimum resolution of the local Jeans length, local density gradients, local pressure gradients, local energy gradients, shocks, and cooling time. A cell reaching any or all of the user-specified criteria will then be flagged for refinement. Once all cells of a given level have been examined, rectangular solid boundaries are determined which minimally encompass the flagged cells on that level. A refined grid patch is then introduced within each such bounding volume, and the results are interpolated to a higher level of resolution.

In Enzo, resolution of the equations being solved is adaptive in time as well as in space. The timestep in Enzo is satisfied on a level-by-level basis by finding the largest timestep such that the Courant condition (and an analogous condition for the dark matter particles) is satisfied by every cell on that level. All cells on a given level are advanced using the same timestep. Once a level  $L$  has been advanced in time  $\Delta t_L$ , all grids at level  $L + 1$  are advanced, using the same criteria for timestep calculations described above, until they reach the same physical time as the grids at level  $L$ . At this point grids at level  $L + 1$  exchange baryon flux information with their parent grids, providing a more accurate solution on level  $L$ . Cells at level  $L + 1$  are then examined to see if they should be refined or de-refined, and the entire grid hierarchy is rebuilt at that level (including all more highly refined levels). The timestepping and hierarchy rebuilding processes are repeated recursively on every level to the maximum existing grid level in the simulation.

Two different hydrodynamic methods are implemented in Enzo: the piecewise parabolic method (PPM) (Woodward & Colella 1984), which was extended to cosmology by Bryan et al. (1995), and the hydrodynamic method used in the ZEUS magnetohydrodynamics code (Stone & Norman 1992a, 1992b). We direct the interested reader to the papers describing both of these methods for more information, and note that PPM is the preferred choice of hydro method since it is higher-order-accurate and is based on a technique that does not require artificial viscosity, which smoothes shocks and can smear out features in the hydrodynamic flow.

The chemical and cooling properties of primordial (metal-free) gas are followed using the method of Abel et al. (1997) and Anninos et al. (1997). This method follows the non-equilibrium evolution of a gas of primordial composition with 9 total species:  $H$ ,  $H^+$ ,  $He$ ,  $He^+$ ,  $He^{++}$ ,  $H^-$ ,  $H_2^+$ ,  $H_2$ , and  $e^-$ . The code also calculates radiative heating and cooling following atomic line excitation, recombination, collisional excitation, free-free transitions, molecular line cooling, and Compton scattering of the cosmic microwave background, as well as any of approximately a dozen different models for a metagalactic ultraviolet background that heat the gas via photoionization and/or photodissociation. We model the cooling processes detailed in Abel et al. (1997), but use the Galli & Palla (1998) molecular hydrogen

cooling function. The multispecies rate equations are solved out of equilibrium to properly model situations where, e.g., the cooling time of the gas is much shorter than the hydrogen recombination time. A total of 9 kinetic equations are solved, including 29 kinetic and radiative processes, for the 9 species mentioned above. The chemical reaction equation network is technically challenging to solve due to the huge range of reaction time scales involved; the characteristic creation and destruction time scales of the various species and reactions can differ by many orders of magnitude. As a result, the set of rate equations is extremely stiff, and an explicit scheme for integration of the rate equations can be costly if small enough timestep are taken to keep the network stable. This makes an implicit scheme preferable for such a set of equations, and Enzo solves the rate equations using a method based on a backwards differencing formula (BDF) in order to provide a stable and accurate solution.

It is important to note the regime in which this chemistry model is valid. According to Abel et al. (1997) and Anninos et al. (1997), the reaction network is valid for temperatures between  $10^0 - 10^8$  K. The original model discussed in these two references is only valid up to  $n_H \sim 10^4 \text{ cm}^{-3}$ . However, addition of the 3-body  $\text{H}_2$  formation process allows correct modeling of the gas chemistry up until the point where collisionally induced emission from molecular hydrogen becomes an important cooling processes, which occurs at  $n_H \sim 10^{14} \text{ cm}^{-3}$ . We do not include heating by molecular hydrogen formation, which will be significant at densities of  $\sim 10^8 \text{ cm}^{-3}$  and above, and may affect temperature evolution at these high densities. A further concern is that the optically thin approximation for radiative cooling breaks down beginning at  $n_H \simeq 10^{10} - 10^{12} \text{ cm}^{-3}$ . Beyond this point, modifications to the cooling function that take into account the non-negligible opacity of the gas to line radiation from molecular hydrogen must be made, as discussed by Ripamonti & Abel (2004). Even with these modifications, a more correct description of the cooling of gas of primordial composition at high densities will require some form of radiation transport, which will greatly increase the cost of the simulations.

## 2.2. Simulation setup

The simulations discussed in this paper are set up in a similar way to those in Paper I. A dark matter-only calculation with  $128^3$  particles in a three-dimensional simulation volume which is  $0.6 \text{ h}^{-1} \text{ Mpc}$  (comoving) on a side is set up at  $z = 99$  assuming a “concordance” cosmological model with no baryons:  $\Omega_m = \Omega_{DM} = 0.3$ ,  $\Omega_b = 0.0$ ,  $\Omega_\Lambda = 0.7$ ,  $h = 0.7$  (in units of  $100 \text{ km/s/Mpc}$ ),  $\sigma_8 = 0.9$ , and using an Eisenstein & Hu power spectrum (Eisenstein & Hu 1999) with a spectral index of  $n = 1$ . The cold dark matter cosmological model is assumed. This calculation is then evolved to  $z = 15$  using a maximum of four levels of

adaptive mesh refinement, refining on a dark matter overdensity of 8.0. At  $z = 15$ , the Hop halo finding algorithm (Eisenstein & Hut 1998) is used to find the most massive halo in the simulation.

At this point, we generate a new set of initial conditions which contain the same large-scale power as the dark matter-only calculation, but include both dark matter and baryons such that the Lagrangian volume in which the halo in the dark matter-only calculation formed is resolved at high spatial and mass resolution using a series of static nested grids, with a  $128^3$  root grid and three static nested grids, for an overall effective root grid size of  $1024^3$  cells. The highest resolution grid is  $256^3$  grid cells, and corresponds to a volume  $150 \text{ h}^{-1}$  comoving kpc on a side. The dark matter particles in the highest resolution grid are  $14.48 \text{ h}^{-1} M_\odot$  and the spatial resolution of the highest resolution grid is  $586 \text{ h}^{-1}$  parsecs (comoving). Previous work shows that this particle mass resolution is adequate to fully resolve the collapse of the halo (Abel et al. 2002; O’Shea & Norman 2007).

All simulations are performed using the adaptive mesh cosmology code Enzo, which is described in Section 2.1. The simulations are started at  $z = 99$  and allowed to evolve until the collapse of the gas within the center of the most massive halo, assuming the presence of an unevolving soft UV background with intensities in the Lyman-Werner band of  $J_{LW} = 0, 10^{-24}, 10^{-23.5}, 10^{-22.5}, 10^{-22}, 10^{-21.67}, 10^{-21.33}$ , and  $10^{-21} \text{ erg s}^{-1} \text{ cm}^{-2} \text{ Hz}^{-1} \text{ sr}^{-1}$ . This range covers a much wider range of parameter space than the results described in Machacek et al. (2001), and completely encompasses the range of possible  $J_{LW}$  values suggested by Wise & Abel (2005), for a wide range of mean Population III stellar masses. Note that many publications use  $F_{LW}$  instead of  $J_{LW}$ :  $F_{LW}$  has units of  $\text{erg s}^{-1} \text{ cm}^{-2} \text{ Hz}^{-1}$ , and thus  $F_{LW} = 4\pi J_{LW}$ . We will use  $J_{LW}$  throughout this paper, and for convenience express values in units of  $J_{21}$ , where  $J_{21}$  is the mean intensity of the UV background in the LW band in units of  $10^{-21} \text{ erg s}^{-1} \text{ cm}^{-2} \text{ Hz}^{-1} \text{ sr}^{-1}$ .

The equations of hydrodynamics are solved using the PPM method with a dual energy formulation, which is required to adequately resolve the thermal properties of gas in high-Mach flows. The nonequilibrium chemical evolution and optically thin radiative cooling of the primordial gas is modeled as described in Section 2.1, following 9 separate species including molecular hydrogen (but excluding deuterium), with an initial electron fraction of  $2.35 \times 10^{-4}$  (which is roughly consistent with Peebles (1968) for an  $\Omega_m = 0.3$ ,  $\Omega_b = 0.04$  universe). Note that the initial electron fraction in the calculation is relatively unimportant to the molecular hydrogen formation rates in halo cores, as the electron fraction at the center of a given halo is controlled primarily by mergers and the shock formed by accretion of gas onto the halo.

Adaptive mesh refinement is used throughout the innermost high resolution region such

that cells are refined by factors of two along each axis, with a maximum of 22 total levels of refinement. This corresponds to a maximum spatial resolution of  $115 \text{ h}^{-1} \text{ AU}$  (comoving) at the finest level of resolution, with an overall spatial dynamical range of  $5.37 \times 10^8$ . To avoid effects due to the finite size of the dark matter particles, the dark matter density is smoothed on a comoving scale of  $\sim 0.5 \text{ pc}$  (which corresponds to  $\simeq 0.03 \text{ proper pc}$  at  $z \simeq 18$ ). This is reasonable because at that scale in all of our calculations the gravitational potential in the halo of interest is completely dominated by the baryons.

Grid cells are adaptively refined based upon several criteria. We refine on baryon and dark matter overdensities in cells of 4.0 and 8.0, respectively. This corresponds to a maximum mass of gas or dark matter per cell (on the most highly refined static grid) of  $M_{\text{max}} = 12.78$  and  $166.16 \text{ M}_{\odot}$ , respectively. In addition, the *MinimumMassForRefinementLevelExponent* parameter is set to  $-0.2$  for both the dark matter and baryon overdensity refinement criteria, meaning that the mass required to refine to a higher level decreases as a function of increasing level, as:

$$M_{\text{ref}}(L) = M_{\text{max}} \times 2^{-0.2L} \quad (1)$$

where  $L$  is the current level of refinement. The negative exponent means that the mass resolution in the calculations is super-Lagrangian – for example,  $M_{\text{ref}}(L = 20) = 0.0625 M_{\text{ref}}(L = 0)$ . In addition to refining on baryon and dark matter overdensity, these simulations include refinement criteria which ensure that shocks are always well-resolved, that the cooling time in a given cell is always longer than the sound crossing time of that cell, and that the Jeans length is always resolved by at least 16 cells. This last criterion guarantees that the Truelove criterion (Truelove et al. 1997) is always resolved by a factor of four more cells in each dimension than is strictly necessary, ensuring that no artificial fragmentation will take place.

### 3. Mean halo properties at collapse

Figures 1 and 2 show projections of baryon density and temperature for the  $J_{21} = 0$  and  $J_{21} = 1$  calculations, respectively, at the epoch at which each calculation collapses, defined as the redshift at which the baryon number density reaches  $\simeq 10^{10} \text{ cm}^{-3}$ . Note that due to the rapid evolution of gas at high density, the “collapse redshift” depends very weakly on the exact choice of density threshold. The calculations are started from the same set of initial conditions, and the  $J_{21} = 1$  calculation is clearly a later stage in the evolution of the  $J_{21} = 0$  run. The satellite halos surrounding the primary halo which collapses at  $z=24.12$



in the  $J_{21} = 0$  run have merged by  $z=17.32$  when the halo in the  $J_{21} = 1$  case collapses (cf. Fig. 8). With virial masses of  $5.68 \times 10^5 M_\odot$  and  $1.26 \times 10^7 M_\odot$ , respectively, the latter halo is more than 20 times as massive as the former. Though quite different in mass, both halos exhibit similar morphologies – they are extremely centrally-concentrated, and only a single condensed object (that is to say, a primordial protostellar cloud core) is visible in the highest-resolution panel in each image. The existence of a single cloud core is common to all calculations discussed in this paper.

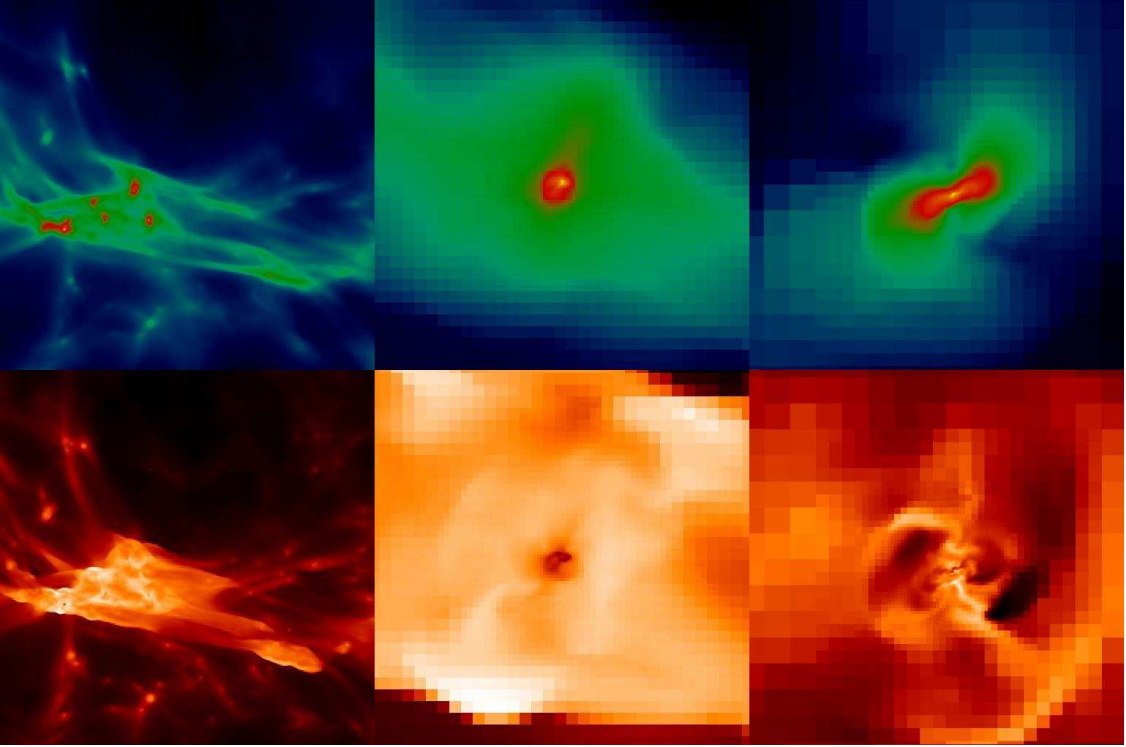


Fig. 1.— Projections of baryon density and temperature at the final output of the  $J_{21} = 0$  simulation ( $z = 24.119$ ;  $M_{vir} = 5.68 \times 10^5 M_{\odot}$ ). Top row: Projected log baryon density. Bottom row: Projected, mass-weighted log baryon temperature. Left column: Region 2.13 kpc (proper) across and deep. Middle column: Region 133.3 pc (proper) across and deep. Right column: Region 0.130 pc (proper) across and deep. The middle and right column are zoomed images focusing on the high baryon density core which forms in the center of the halo.

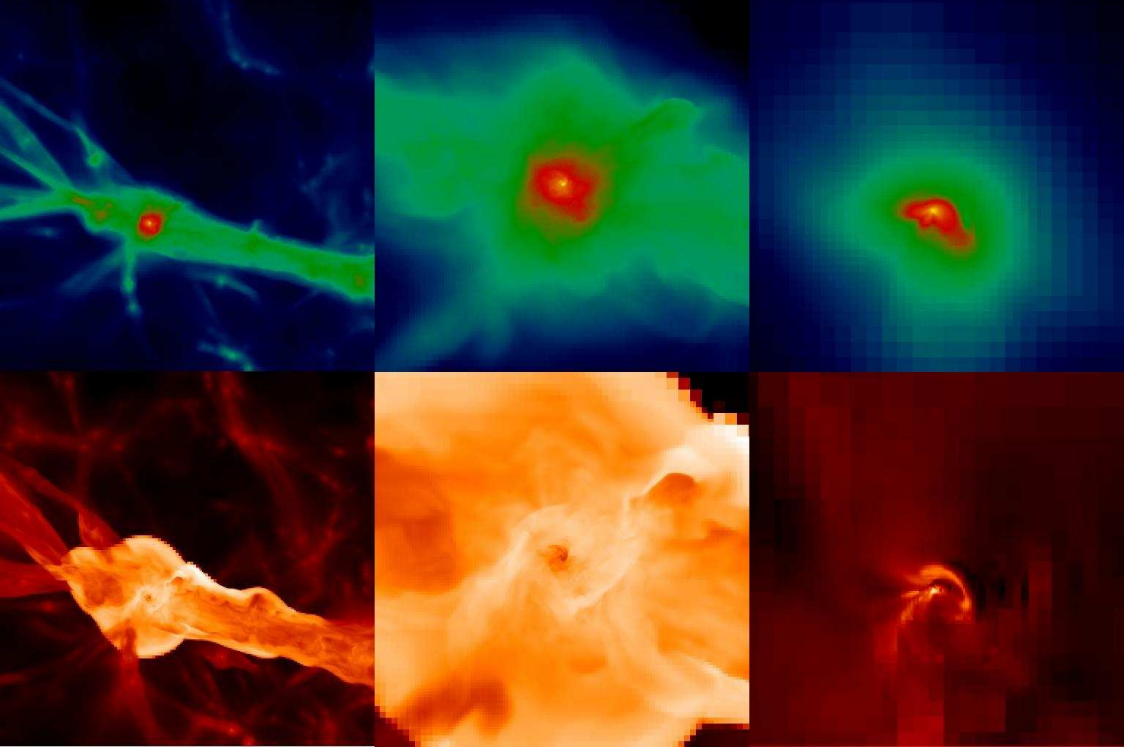


Fig. 2.— Projections of baryon density and temperature at the final output of the  $J_{21} = 1$  simulation ( $z = 17.322$ ;  $M_{vir} = 1.260 \times 10^7 M_{\odot}$ ). Top row: Projected log baryon density. Bottom row: Projected, mass-weighted log baryon temperature. Left column: Region 2.13 kpc (proper) across and deep. Middle column: Region 533 pc (proper) across and deep. Right column: Region 0.260 pc (proper) across and deep. The middle and right column are zoomed images focusing on the high baryon density core which forms in the center of the halo.

Figure 3 shows several mean halo quantities for all simulations discussed in this paper, including halo collapse redshift as a function of  $J_{LW}$ , virial mass as a function of  $J_{LW}$ , virial temperature as a function of  $J_{LW}$ , and the virial mass as a function of collapse redshift. Simulations where the soft UV background is turned on are shown by solid squares, and the “control”  $J_{21} = 0$  calculation is shown by an open square. In plots where  $J_{LW}$  is shown on the x-axis, the  $J_{21} = 0$  simulation is placed at  $\log_{10} J_{LW} = -24.5$ .

Figure 3 shows that there is a clear relationship between the LW intensity and the collapse redshift and virial mass of the halo. A larger LW intensity results in a later collapse time and larger virial mass because the halo must be hotter in order to have a cooling time which is less than a Hubble time despite the depressed  $H_2$  abundance in the high-density gas at the halo’s center. This is discussed further in Section 4. The final mass of the halos in the simulations with  $J_{21} = 1$  is approximately a factor of 20 higher than that in the “control” simulation. This is in qualitative agreement with Machacek et al. (2001), who suggest that there is a “minimum halo mass” as a function of the strength of the LW background of the form

$$M_{TH}(M_{\odot}) = 1.25 \times 10^5 + 8.7 \times 10^5 \left( \frac{F_{LW}}{10^{-21}} \right)^{0.47}, F_{LW} \leq 10^{-21} \quad (2)$$

This threshold mass is plotted in panel (c) of Figure 3. Eq. 2 is only strictly valid over the range  $0 \leq F_{LW} = 4\pi J_{LW} \leq 10^{-21}$ , because this was the range simulated by Machacek et al. (2001). We see that our points for  $J_{21} \leq 0.1$  parallel the threshold curve but at a mass approximately four times higher. This difference can be ascribed to two factors. First, the threshold mass is the lowest possible halo mass that can collapse, derived from a statistical sample. Since we study only one realization which focuses on the most massive halo in the box, its mass is bound to be higher than the statistical minimum. Second, Machacek et al. (2001)’s criterion for cooling catches halos at an earlier stage of evolution compared to our data points, which give the halos’ virial masses at the time of central baryon collapse (the “collapse redshift”).

Examination of panels (b) and (c) of Figure 3 show that there is some sort of “phase change” between  $J_{21} = 10^{-1.5}$  and  $10^{-1}$  causing the halo mass at the time of collapse to increase steeply and non-monotonically. The collapse redshift steadily decreases as a function of UV increasing background strength (i.e. collapse of gas at the center of the halo is delayed). However, panel (c) shows that the virial mass steadily increases with increasing UV background strength until  $J_{21} = 10^{-1.5}$ , at which point there is a jump in mass by more than a factor of four, above which the halo mass increases only slightly with increasing UV background strength. That something interesting should happen at these LW intensities is

consistent with the findings of Yoshida et al. (2003) who found that  $\text{H}_2$  cooling is strongly suppressed at  $J_{21} = 0.1$ . They predicted that star formation would be inhibited since the equilibrium  $\text{H}_2$  fraction is below the critical fraction for cooling derived by Tegmark et al. (1997). Contrary to these predictions, we find collapse not only at  $J_{21} = 0.1$ , but also at values as large as  $J_{21} = 1$ . We note that highest value considered by Machacek et al. (2001) was  $J_{21} = 0.0796$ , and the highest simulated by Yoshida et al. (2003) was  $J_{21} = 0.1$ . Therefore our cases  $J_{21} > 0.1$  have not been examined before, and certainly not at the resolution of our simulations.

How is the gas in the center of these halos able to cool and collapse in such high radiation backgrounds? This is analyzed in some detail in the next section. A hint is provided in (d) of Figure 3, which plots the halo virial temperature as a function of  $J_{LW}$ . At background strengths above  $J_{21} = 10^{-1.5}$ , the virial temperature is consistently approximately  $10^4$  K, which is roughly the temperature at which atomic hydrogen cooling is effective. However, an examination of the radial temperature profiles shows that high-density gas in the center of the halo never reaches these temperatures, but is more typically 2000 K. Atomic line cooling is unimportant at such low temperatures; however the  $\text{H}_2$  cooling rate per particle is roughly 100 times as large at 2000K as at 500K.  $\text{H}_2$  cooling still operates in the halo centers despite low  $\text{H}_2$  abundance due to the higher cooling rates and long evolutionary timescales. In the rest of this section we merely present additional mean properties of the halo and its central region at collapse, and defer discussion of the relevant timescales to Section 4.

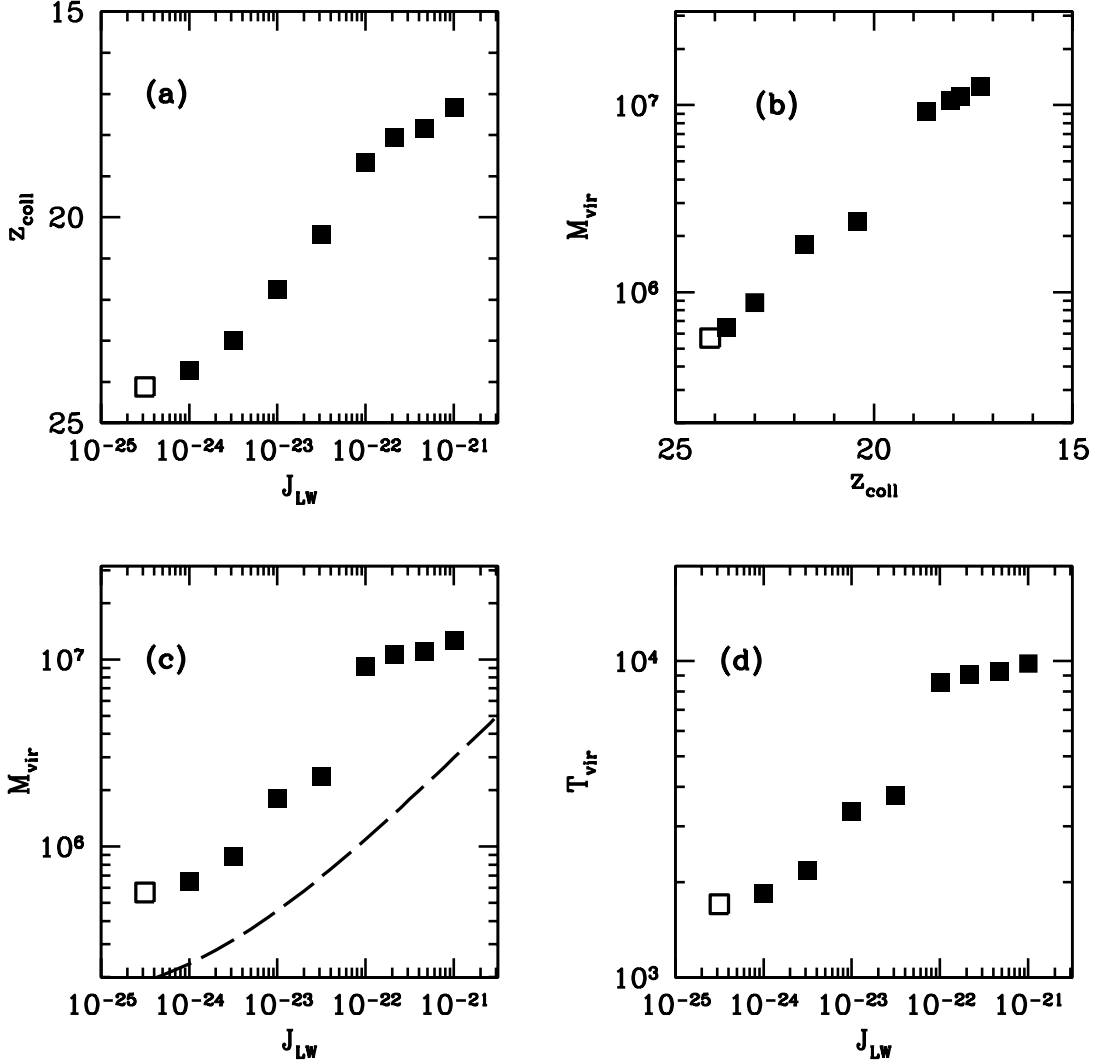


Fig. 3.— Mean halo quantities for several simulations with the same cosmic realization but a range of Lyman-Werner molecular hydrogen photodissociating flux backgrounds. Panel (a):  $J_{LW}$  vs. halo collapse redshift. Panel (b): halo virial mass vs. halo collapse redshift. Panel (c): halo virial mass vs.  $J_{LW}$ . Panel (d): halo virial temperature vs.  $J_{LW}$ . The  $J_{21} = 0$  “control” result are shown as an open square (and is at  $\log J_{LW} = -24.5$  in the panels which are a function of  $J_{LW}$ ). In the bottom left panel, the dashed line corresponds to the fitting function for threshold mass from Machacek et al. (2001), Eqn. 8.

Figure 4 shows several properties of the halo core at the epoch of collapse, including the core temperature, molecular hydrogen fraction, and spherically-averaged accretion rate as a function of ultraviolet background strength, and the spherically-averaged accretion rate as a function of the molecular hydrogen fraction. All “core” values are spherically-averaged and measured at the mass shell where  $100 M_{\odot}$  of gas is enclosed. Panel (a) shows that the core  $H_2$  fraction decreases significantly with increasing FUV flux, with a corresponding increase in the core temperature (Panel (b)). This relationship is similar to that noted in O’Shea & Norman (2007), where the amount of molecular hydrogen at densities of  $10^4 - 10^8 \text{ cm}^{-3}$  varies between simulations, and correlates strongly with baryon temperature. Given that the accretion of gas onto the protostellar cloud is subsonic, this results in a strong relationship between the soft UV background flux and accretion rate onto the protostellar cloud, as shown by Panel (c), with accretion rates varying by more than a factor of 30 between the  $J_{21} = 0$  and 1 cases. Panel (d) shows the strength of the correlation between core  $H_2$  fraction and accretion rate. Note that the values discussed above are insensitive to the exact definition of the halo “core.”

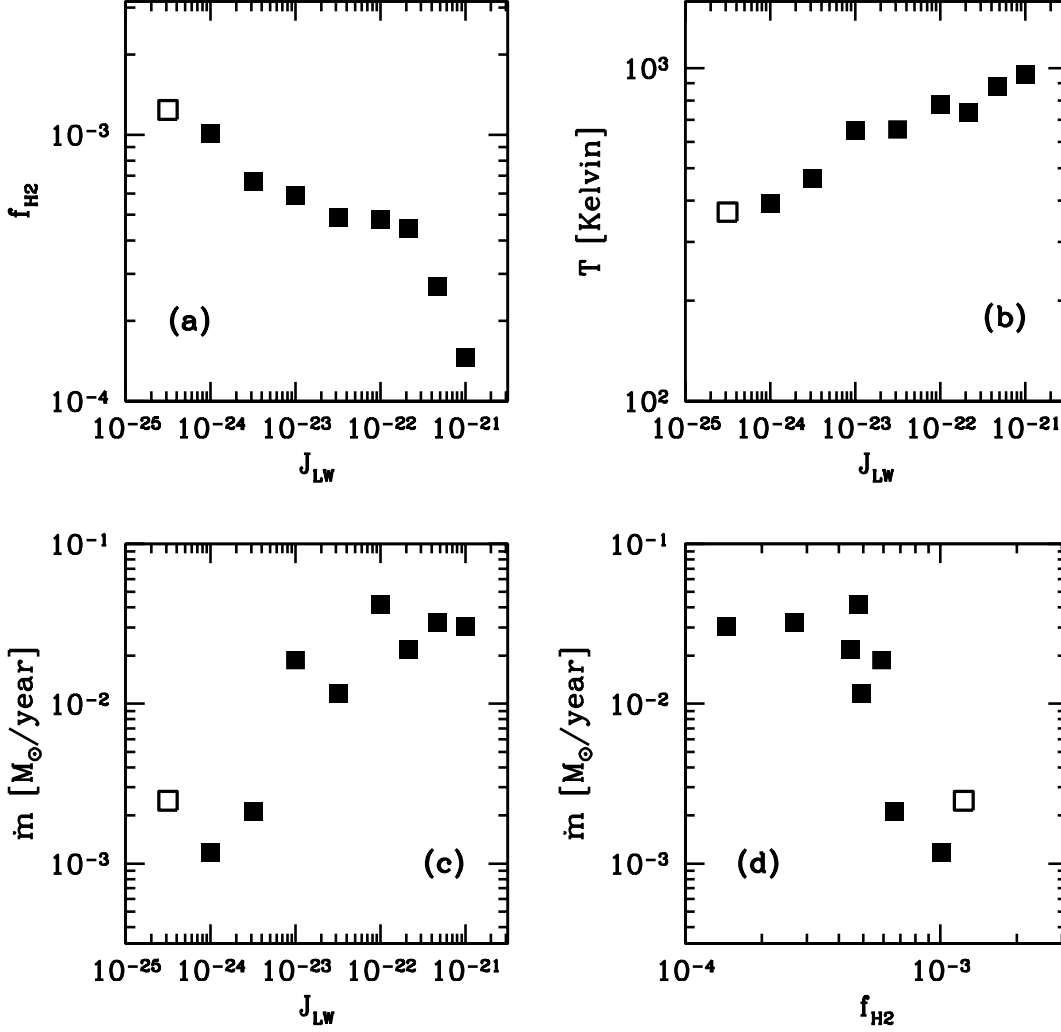


Fig. 4.— Mean quantities within the central  $100M_{\odot}$  core for several simulations with the same cosmic realization but a range of LW background intensities. Panel (a):  $J_{\text{LW}}$  vs. baryon core temperature. Panel (b):  $J_{\text{LW}}$  vs. baryon core  $H_2$  fraction. Panel (c):  $J_{\text{LW}}$  vs. instantaneous accretion rate. Panel (d): Baryon core  $H_2$  fraction vs. accretion rate. The  $J_{21} = 0$  “control” result are shown as an open square (and is at  $\log J_{\text{LW}} = -24.5$  in the panels which are a function of  $J_{\text{LW}}$ ). All “core” values are spherically-averaged and measured at the mass shell where  $100 M_{\odot}$  of gas is enclosed.



Figure 5 shows the halo core mass and mass fraction at the epoch of collapse (note that the definition of “core” is somewhat different than in the previous figure). The halo “core mass” is defined as being all gas at a density of  $n_H = 10^4 \text{ cm}^{-3}$  or above, and the core mass fraction is defined as the core mass divided by the virial mass of the halo at the epoch of collapse. This choice of minimum density ensures that we have captured the entirety of the quasistatically contracting analog of a galactic molecular cloud core, and for practical purposes is comparable to the gas fraction of cold, dense gas discussed in Machacek et al. (2001). The size of the halo core increases in absolute terms as the strength of the photodissociating background is increased, from  $\simeq 10^3 M_\odot$  until  $J_{21} = 0.1$ , where it reaches  $\simeq 11,000 M_\odot$ . Above this value of  $J_{21}$ , the core mass then begins to decrease, reaching  $\simeq 7600 M_\odot$  at  $J_{21} = 1$ . The core mass fraction generally decreases (though with some noise in the relationship) from  $\simeq 1.7 \times 10^{-3}$  at  $J_{21} = 0$  to  $\simeq 6.96 \times 10^{-4}$  at  $J_{21} = 1$ , though the total overall change is less than a factor of 2.

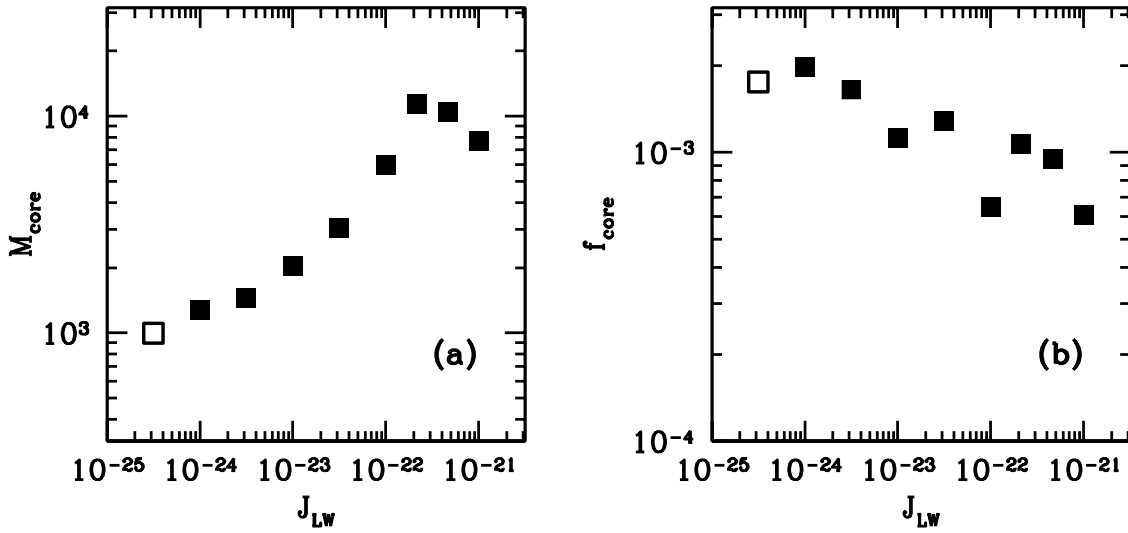


Fig. 5.— Halo core mass (Panel (a)) and core mass fraction (Panel (b)) for several simulations with the same cosmic realization but a range of LW background intensities. The “core mass” is defined as the mass of gas in the halo which has a density of  $n_H = 10^4 \text{ cm}^{-3}$  or above. The “core mass fraction” is defined as the “core mass” divided by the virial mass of the halo at the epoch of collapse. The  $J_{LW} = 0$  “control” result are shown as an open square (and is at  $\log J_{LW} = -24.5$  in the panels which are a function of  $J_{LW}$ ).

#### 4. Central evolution prior to collapse

We now examine in more detail the evolution of the conditions in the cloud center leading to collapse. In Figure 6 we plot the central density, temperature, entropy  $S \equiv T/n_H^{2/3}$ , and  $H_2$  fraction versus time for the calculations with  $J_{21} = 10^{-3}$  (solid line),  $10^{-2}$  (short-dashed line),  $10^{-1}$  (long-dashed line) and 0 (dot-dashed line). In these plots, central values of temperature and density are defined as being the values of these quantities in the cell with the highest baryon density. It is most instructive to compare the two extreme cases,  $J_{21} = 10^{-3}$ , which very closely resembles the  $J_{21} = 0$  case, and the  $J_{21} = 1$  case, which according to Yoshida et al. (2003) should not collapse at all. In panel (a) we see the central density increase modestly from  $\sim 2 \text{ cm}^{-3}$  to  $\sim 20 \text{ cm}^{-3}$  over 40 Myr, and then increase rapidly thereafter, reaching  $10^8 \text{ cm}^{-3}$  in a scant additional 15 Myr. This evolution is driven by  $H_2$  cooling, as can be seen from the entropy evolution in panel (c). As expected, runaway cooling occurs when the  $H_2$  fraction reaches  $\sim 2 \times 10^{-4}$  (panel d), consistent with the Tegmark et al. (1997) analysis. By contrast the  $J_{21} = 1$  case requires 120 Myr for the central density to increase from  $\sim 2 \text{ cm}^{-3}$  to  $\sim 20 \text{ cm}^{-3}$ . As shown in panel (c), the first 50 Myr of this contraction is adiabatic, followed by an increase in entropy due to some heating event (mergers). The fact that central entropy is not decreasing for 90 Myr is indicative of the fact that  $H_2$  cooling is unimportant over this interval due to extremely low equilibrium  $H_2$  fractions ( $f_{H_2} < 10^{-6}$ ; (panel d)).

However, something interesting happens in the  $J_{21} = 1$  calculation at  $t \approx 170$  Myr. Prior to that time the central temperature has crept up to 5000 K due to the increased virial mass. The cooling rate per  $H_2$  molecule is about 3 orders of magnitude higher at 5000K than at 500K – a typical temperature at the halo center in low UV background evolutions. We believe this high temperature is due to a combination of adiabatic heating as the potential well deepens, and merger-induced shock heating. As shown in Figure 8, three large halos merge between  $z = 20$  and  $z = 18$ , quadrupling the halo mass (Figure 3, panel (b)). The elevated cooling rates cool the gas at the halo center to  $T \approx 2000 \text{ K}$ , allowing the gas density to increase slightly. The two effects reduce the central entropy from  $S \approx 700 \text{ K cm}^2$  to  $\approx 250 \text{ K cm}^2$ . This is followed by another heating event at  $t=190$  Myr, presumably due to another merger, followed by a second more catastrophic cooling event. At  $t=200$  Myr, the halo core collapses, driving the central density higher, temperature and entropy lower, and  $H_2$  fraction higher.

Why does this collapse occur? This is analyzed in Figure 7, where we plot the evolution of the important timescales in the center of the halo. In the  $J_{21} = 10^{-3}$  case, the 2-body  $H_2$  formation timescale is always roughly an order of magnitude smaller than the photodissociation timescale. Consequently, the  $H_2$  abundance is out of equilibrium and grows steadily

with time (Figure 6 panel d). The  $H_2$  cooling time in the central zone ( $\leq 1$  Myr) is far less than the Hubble time ( $\sim 100$  Myr), and before too long runaway collapse occurs. At higher values of  $J_{LW}$ , the 2-body  $H_2$  formation time always hovers around the photodissociation timescale, regardless of how long that timescale is. This tells us that  $H_2$  is in equilibrium: the 2-body formations balance the photo-destructions by the LW background. The equilibrium  $H_2$  fraction is given by

$$f_{H_2} \approx \frac{k_{H^-} n_e}{k_{diss}} \quad (3)$$

where  $k_{H^-}$  is the rate coefficient for the formation of  $H^-$  (the limiting reaction for  $H_2$  formation at the temperature and density range considered here),  $n_e$  is the electron density, and  $k_{diss} = 1.1 \times 10^8 F_{LW} s^{-1}$  is the  $H_2$  photodissociation rate due to the Solomon process (Abel et al. 1997; Yoshida et al. 2003). Using  $T = 2000$  K and  $n_e = 10^{-4}$ , we get  $f_{H_2} = 1.46 \times 10^{-6} \left(\frac{F_{LW}}{10^{-21}}\right)^{-1}$ , which is in good agreement with the  $H_2$  fractions we see in Figure 6. Since  $t_{H_2} \equiv n_{H_2} / \dot{n}_{H_2} \propto f_{H_2}$ , the smaller  $f_{H_2}$  is, the shorter its formation time.

Now let us consider the  $H_2$  cooling time evolution (short-long-dashed line). It is far less than a Hubble time for  $J_{21} \leq 10^{-1}$ , ensuring that these halo cores will eventually cool and collapse. In the  $J_{21} = 1$  case, the cooling time drops below the Hubble time for the first time at  $t=170$  Myr, and again at  $t=190$  Myr where it begins a steady decrease toward  $10^6$  yr. Despite the low equilibrium  $H_2$  fraction, if we wait long enough the inexorable press of time eventually establishes the condition  $t_{cool} < t_{Hubble}$  and we get runaway collapse, even for  $J_{21} = 1$ . Note that we get catastrophic cooling because we are in the density regime ( $n < 10^4 \text{ cm}^{-3}$ ) where  $H_2$  cooling is proportional to the square of the gas density, not linear in the gas density (Abel, Bryan, & Norman 2000; Abel et al. 2002).

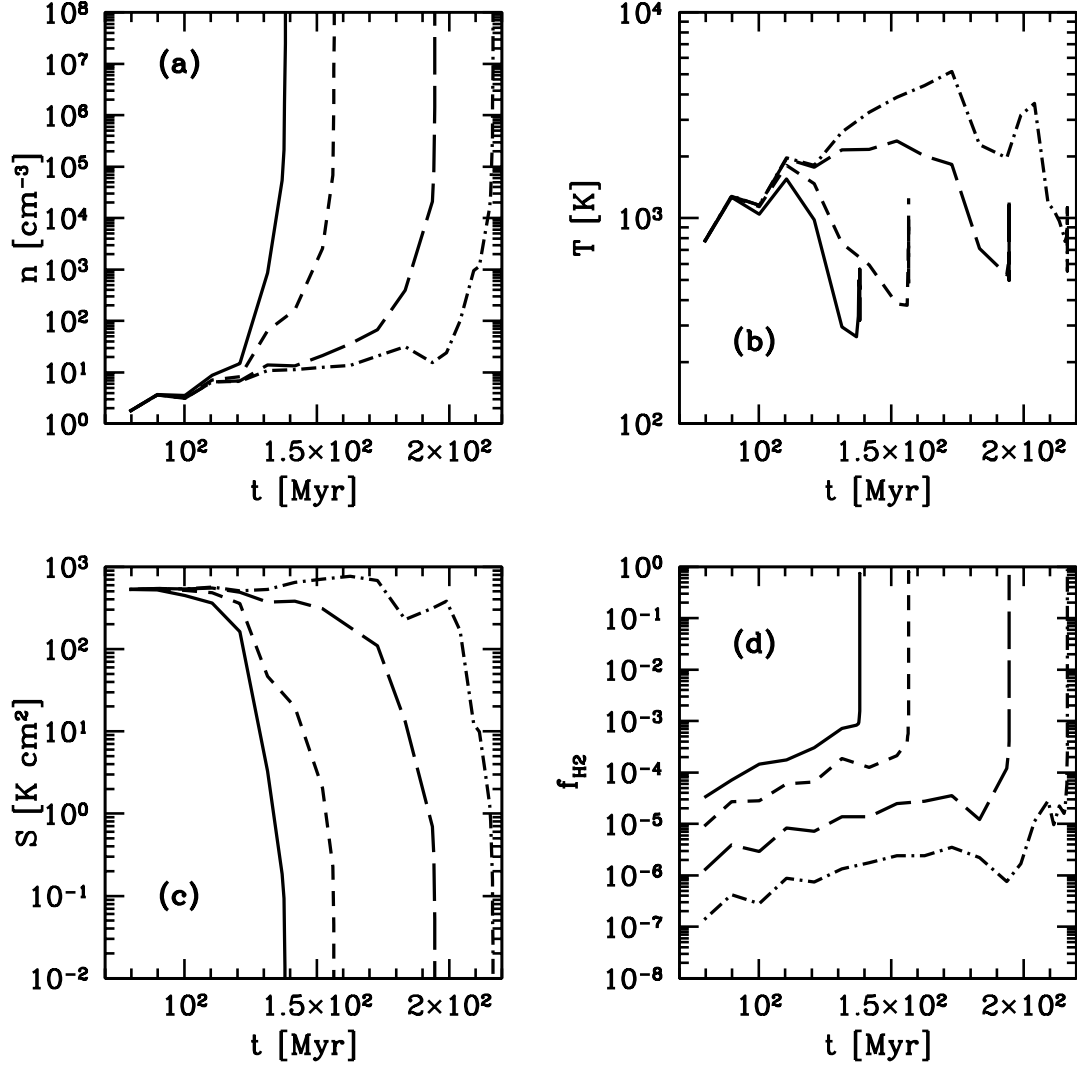


Fig. 6.— Evolution of the central density (Panel (a)), temperature (Panel (b)), entropy (Panel (c)), and H $_2$  fraction (Panel (d)) as a function of time for the cases  $J_{21} = 10^{-3}$  (solid),  $10^{-2}$  (short-dashed),  $10^{-1}$  (long-dashed) and  $1$  (dot-dashed).

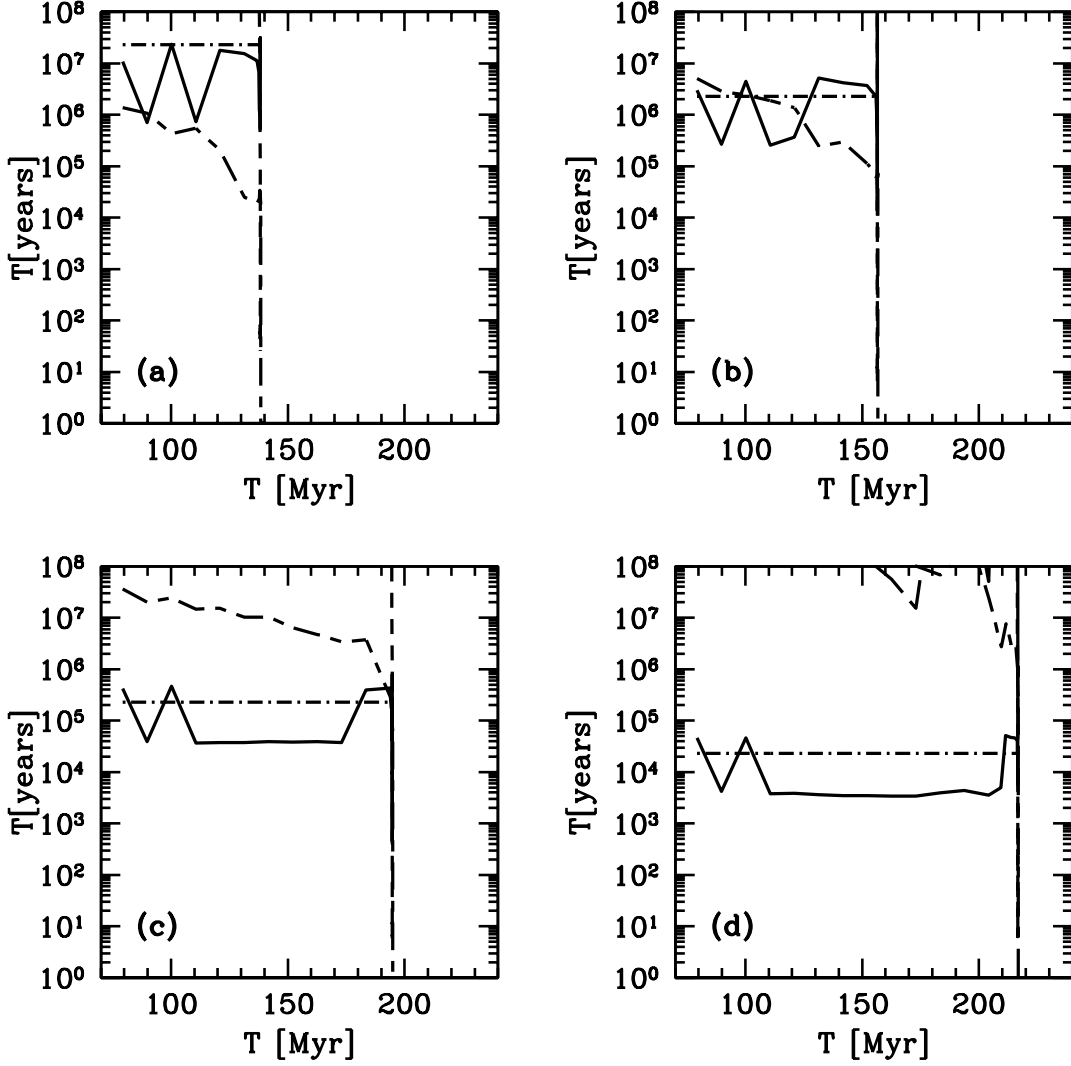


Fig. 7.— Evolution of timescales in the central zone for the cases  $J_{21} = 10^{-3}, 10^{-2}, 10^{-1}$  and 1 (Panels (a)–(d), respectively): 2-body  $\text{H}_2$  formation time (solid); 3-body  $\text{H}_2$  formation time (short-dashed);  $\text{H}_2$  collisional dissociate time (long-dashed);  $\text{H}_2$  photodissociation time (dot-dashed);  $\text{H}_2$  cooling time (short-long-dashed).

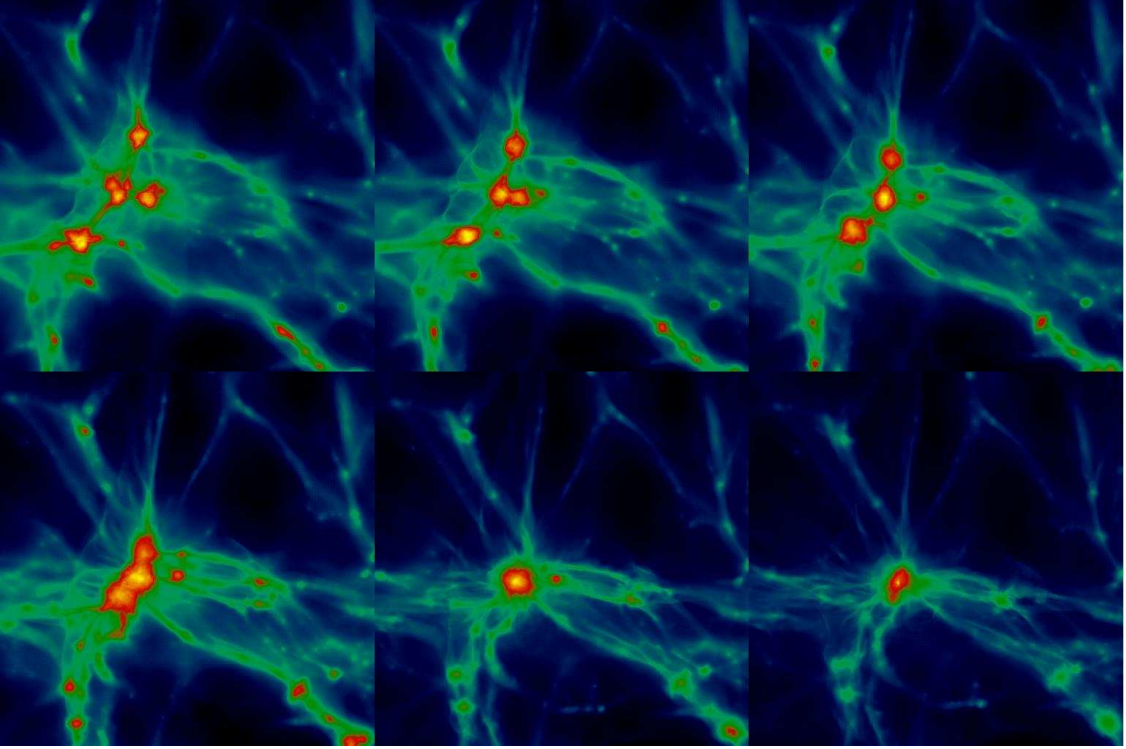


Fig. 8.— Merger history of the  $M_{vir} = 1.26 \times 10^7 M_{\odot}$ ,  $T_{vir} = 10^4$  K halo that collapses at  $z=17.32$  with a Lyman-Werner background flux  $J_{21} = 1$ . In comic strip order, the redshifts are  $z=22, 21, 20, 19, 18$ , and  $17.32$ . Field of view is 53.571 comoving kpc (2.678 proper kpc at  $z = 19$ ). Logarithm of the projected baryon density (column density) is displayed, with color table scaled to the maximum and minimum values in each image.

## 5. Halo properties at the epoch of collapse

Figure 9 shows radial profiles of baryon number density, temperature, enclosed mass, circular velocity, and RMS Mach number as a function of radius, as well as specific angular momentum as a function of enclosed mass, for all simulations discussed in this paper. To facilitate comparison, results from the output of each simulation where the peak baryon number density at the center of the halo is approximately  $10^{10} \text{ cm}^{-3}$  are shown, in order to capture each halo at a similar evolutionary stage, rather than at a fixed point in time. Panel (a) shows that all of the simulations have similar density profiles. The scatter in number density at a given radius is readily explained by variation in halo mass – halos which collapse at later times (due to higher UV background strength) are more massive, and thus have higher overall baryon densities. This is shown in another way in Panel (c), in a plot of enclosed mass as a function of radius which shows that all halos have very similar profiles at  $r \lesssim 10^{-2} \text{ pc}$ , but a significant variation at larger radii which is related to halo mass. The plot of temperature as a function of radius in Panel (b) shows an interesting trend – as the LW background is increased, the overall halo temperature as well as the halo core (where “core” is roughly defined as gas within  $\sim 1 \text{ pc}$  of the halo center) temperature go up. In the outskirts of the halo, where baryon densities are low and thus cooling times are long, this is due primarily to the increase in halo mass, with the peak temperature corresponding approximately to the halo virial temperature. In the halo core, however, this temperature is correlated more strongly with the  $\text{H}_2$  fraction, and thus the UV background, as suggested by Figure 4. The plots of specific angular momentum as a function of enclosed mass and Keplerian velocity fraction (defined as the local circular velocity divided by the Keplerian orbital velocity due to mass within that radius) as a function of radius in panels (d) and (e) show some mild trends. It appears that halos in simulations with stronger UV backgrounds tend to have less specific angular momentum at a given mass shell, and also tend to have a lower Keplerian velocity fraction at a given radius than gas in halos which form in the presence of a lower UV background – indeed, the halo which forms in the  $J_{21} = 1$  calculation has the least angular momentum of all of the simulations, and the lowest Keplerian velocity fraction out to  $\sim 1 \text{ pc}$ . We speculate that this is due to transport and segregation of angular momentum by turbulence – halos whose collapse is delayed have more time for these processes to act within the halo core, resulting in less angular momentum overall when the halo ultimately collapses (note that this will be discussed more fully in a later paper). The plot of RMS Mach number as a function of radius in panel (f) also shows no obvious trend, though at radii below  $\sim 10^{-2} \text{ pc}$ , simulations with a smaller UV background generally have higher RMS Mach numbers. This is due primarily to the gas being colder, and not the gas velocities being higher.



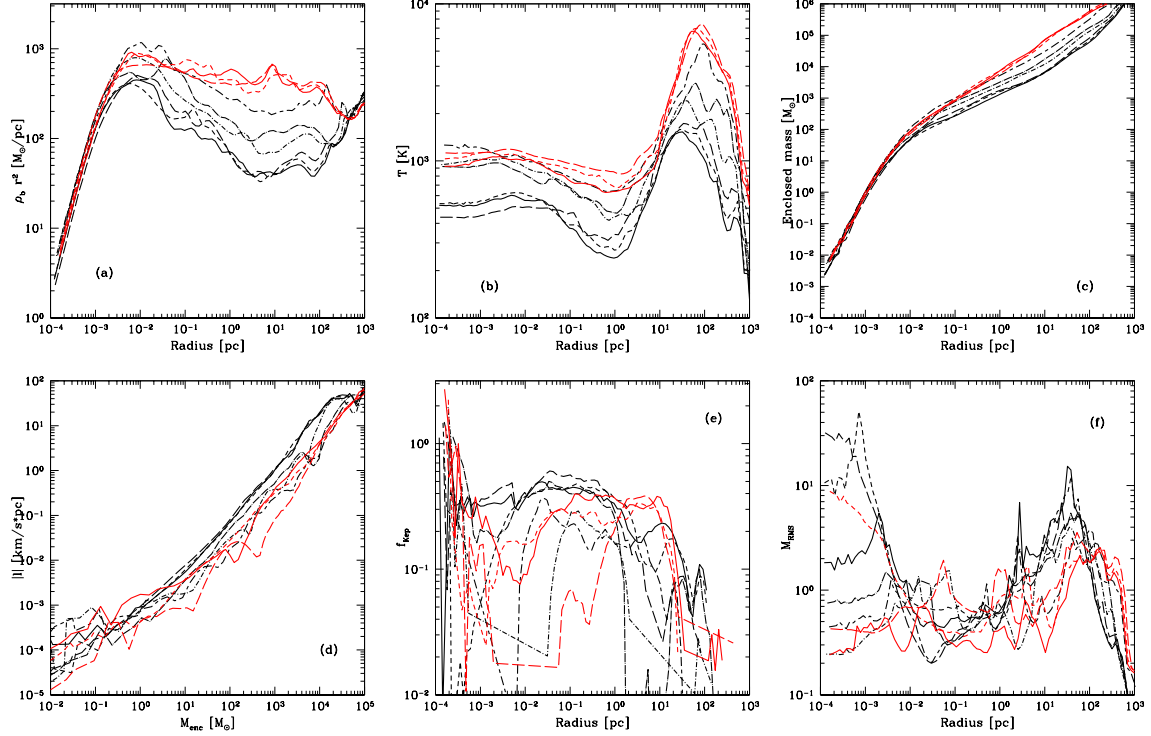


Fig. 9.— Evolution of several spherically-averaged baryon quantities for simulations with all values of  $J_{21}$ . Panel (a):  $\rho_b r^2$  as a function of radius. Panel (b): Temperature as a function of radius. Panel (c): Enclosed gas mass as a function of radius. Panel (d): Specific angular momentum as a function of enclosed mass. Panel (e): Keplerian velocity fraction as a function of radius. Panel (f): Gas RMS Mach number as a function of radius. All quantities except enclosed gas mass are mass-weighted, and all simulations are shown at the point where the maximum number density is approximately  $10^{10} \text{ cm}^{-3}$ . Line types and weights correspond to simulations, as follows. Black solid line:  $J_{21} = 0$ . Black short-dashed line:  $J_{21} = 10^{-3}$ . Black long-dashed line:  $J_{21} = 10^{-2.5}$ . Black dot short-dashed line:  $J_{21} = 10^{-2}$ . Black dot long-dashed line:  $J_{21} = 10^{-1.5}$ . Black short dashed-long dashed line:  $J_{21} = 10^{-1}$ . Red solid line:  $J_{21} = 10^{-0.67}$ . Red short-dashed line:  $J_{21} = 10^{-0.33}$ . Red long-dashed line:  $J_{21} = 1$ .

Figure 10 shows the  $\text{H}_2$  fraction, electron fraction,  $\text{H}^-$  fraction, ratio of cooling time to sound crossing time, ratio of cooling time to dynamical time, and ratio of sound crossing time to dynamical time as a function of radius, for all simulations. Outputs and line types correspond to those in Figure 9. There is a clear relationship at all radii between  $\text{H}_2$  fraction and UV background strength in panel (a) – as the FUV background is increased, the overall  $\text{H}_2$  fraction decreases. This difference is most noticeable at radii of  $0.1 - 10$  pc, but is maintained at larger and smaller radii. There is a “kink” at approximately  $10^{-2}$  pc where the values are all quite similar. This corresponds to a baryon number density of  $\sim 10^8 \text{ cm}^{-3}$  in all simulations, which is where 3-body  $\text{H}_2$  formation begins to occur. Panels (b) and (c) show that  $\text{e}^-$  and  $\text{H}^-$  fractions track each other, which is to be expected – the local electron fraction controls the amount of  $\text{H}^-$  which can be produced, which is the limiting reaction in the dominant mode of  $\text{H}_2$  formation for  $n \lesssim 10^8 \text{ cm}^{-3}$  – and there is a general trend with increasing electron and  $\text{H}^-$  fractions with increasing UV background flux.

The plots of the ratio of cooling time to sound crossing time, ratio of cooling time to dynamical time, and ratio of sound crossing time to dynamical time as a function of radius shown in panels (d), (e) and (f) display some interesting trends. The three simulations with the lowest UV background strengths have a much longer cooling time than the other calculations, which are all grouped roughly together with no discernible pattern. This agrees well with the plot of the ratio of cooling time to dynamical time, where a similar trend is observed. The difference between the three simulations with the lowest UV background strengths and the others is due to the somewhat higher  $\text{H}_2$  fraction in the halo core of these calculations. The gas temperature is  $\sim 200$  K at the center of the halo cores in these calculations, and the gas cannot cool further, which results in a very long cooling time. The sound crossing time is also increased, but not as significantly. All simulations have approximately the same ratio of sound crossing to dynamical times at all radii. Given that the cooling time is typically longer than both the sound crossing time and dynamical time, one can infer that the collapse of the halo is occurring quasi-statically for all simulations.

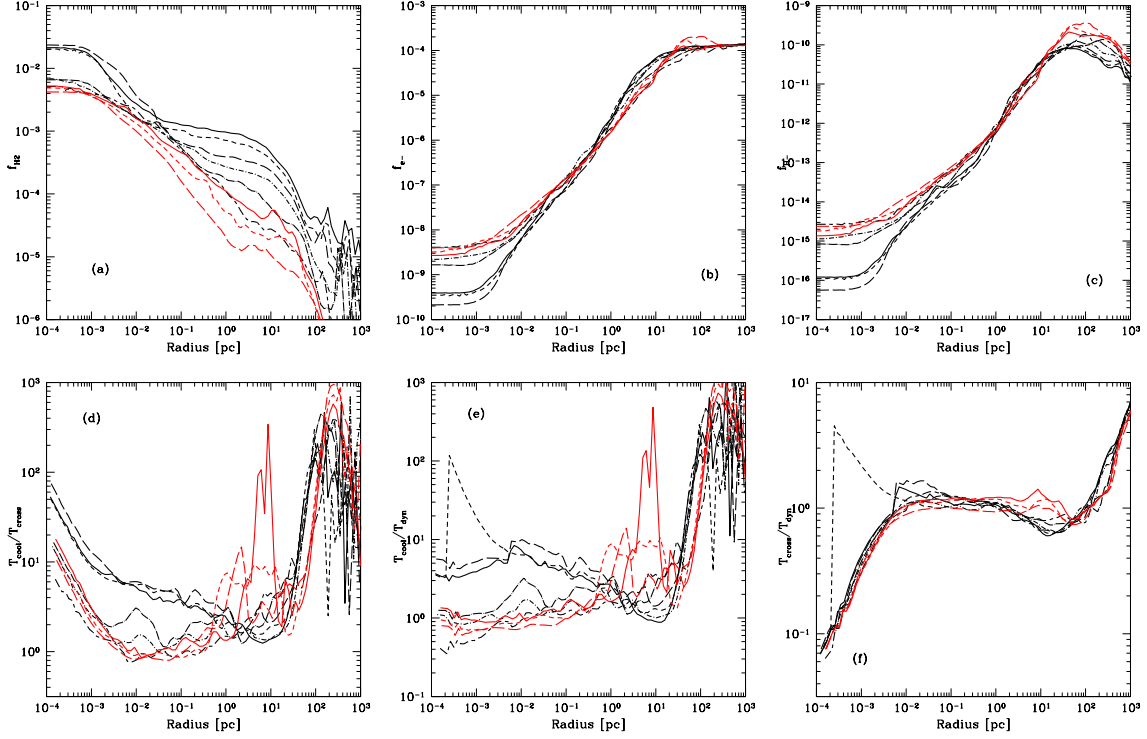


Fig. 10.— Several spherically-averaged baryon quantities for simulations with all values of  $J_{21}$ . Panel (a): Molecular hydrogen fraction as a function of radius. Panel (b): Electron fraction as a function of radius. Panel (c):  $H^-$  fraction as a function of radius. Panel (d): Ratio of gas cooling time to sound crossing time as a function of radius. Panel (e): Ratio of gas cooling time to dynamical time as a function of radius. Panel (f): Ratio of gas sound crossing time to dynamical time as a function of radius. All quantities except enclosed gas mass are mass-weighted, and all simulations are shown at the point where the maximum number density is approximately  $10^{10} \text{ cm}^{-3}$ . Line types and weights correspond to those in Figure 9.

Figure 11 shows radial velocity as a function of radius, accretion time (defined as  $M_{b,enc}/\dot{M}$ ) as a function of enclosed baryon mass  $\dot{M}$  as a function of enclosed baryon mass and  $\dot{M}$  as a function of time for all simulations. Output time and lines correspond to those in Figures 9 and 10. Panel (a) shows a clear relationship between the strength of the soft UV background and the radial velocity, with the calculations that have higher UV backgrounds also having higher infall velocities. This is easily understood by the quasistatic contraction of the gas, which takes place at or below the local sound speed in the gas, as discussed by Abel et al. (2002) and O’Shea & Norman (2007). Given that the halo temperatures are systematically higher in calculations where the UV background is stronger, the sound speed is higher, and thus the rate at which the gas at the center of the halo contracts is higher. This leads to lower accretion times (Panel (b)) and higher accretion rates (Panel (c)), with the accretion rates for the simulations with the strongest UV backgrounds being higher than those with a low (or no) UV background. Panel (d) shows that the time evolution of the accretion rate in all simulations is qualitatively similar, but varies strongly in absolute magnitude and in the time at which the accretion rate onto the evolving protostellar cloud peaks, suggesting that the stars forming in these simulations may have very different evolutionary histories.

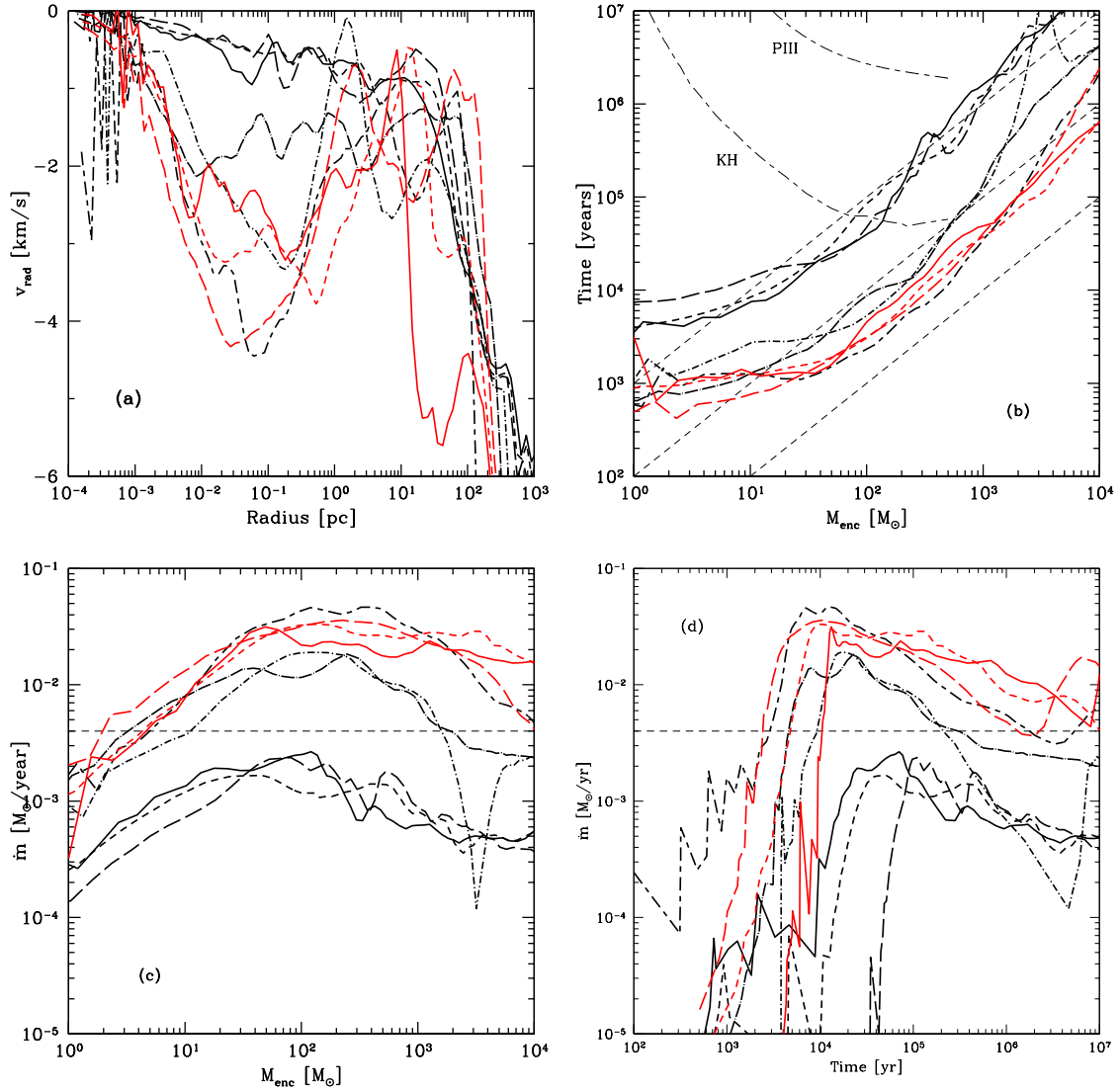


Fig. 11.— Several spherically-averaged baryon quantities for simulations with all values of  $J_{21}$ . Panel (a): Radial velocity as a function of radius. Panel (b): Accretion time as a function of enclosed baryon mass. Panel (c): Instantaneous accretion rate as a function of enclosed baryon mass. Panel (d): Estimated accretion rate as a function of time. All quantities except enclosed gas mass are mass-weighted, and all simulations are shown at the point where the maximum number density is approximately  $10^{10} \text{ cm}^{-3}$ . Line types and weights correspond to those in Figure 9. The upper and lower light short-long-dashed curves which extend from the upper left corner of Panel (b) correspond to the main sequence lifetime of a massive Population III star of that mass and the Kelvin-Helmholtz timescale of a Population III timescale with a given luminosity and radius. All values are taken from Schaerer (2002). The three light diagonal short-dashed lines which extend from bottom left to top right in panel (b) correspond to masses accreted using constant accretion rates of (from top to bottom)  $\dot{m} = 10^{-3}, 10^{-2}$ , and  $10^{-1} M_{\odot}/\text{yr}$ . The light horizontal short-dashed line in panels (c) and (d) correspond to the “critical” accretion rate of Omukai & Palla (2003),  $\dot{m} \simeq 4 \times 10^{-3} M_{\odot}/\text{yr}$ .

## 6. Halo properties at fixed redshift

Figure 12 shows the status of several spherically-averaged quantities for halos from all simulations at a fixed redshift,  $z = 25$ , which is shortly before the baryons in the most massive halo in the  $J_{21} = 0$  simulation collapses to high density. This is at an early point in the evolution of the majority of these halos, and several conclusions can be drawn from the plots of number density, temperature,  $H_2$  fraction, and radial velocity as a function of radius. The molecular hydrogen fraction declines monotonically with increasing UV background strength, in agreement with an estimate for equilibrium  $H_2$  fraction at low ( $n \ll 10^8 \text{ cm}^{-3}$ ) densities:

$$f_{H_2} = \frac{k_{H^-} n_e}{k_{LW}} \quad (4)$$

where  $k_{H^-}$  is the rate coefficient for the formation of  $H^-$  (the limiting reaction for  $H_2$  formation at the temperature and density range considered here) and  $k_{LW}$  is the rate coefficient for  $H_2$  in the LW band (Abel et al. 1997; Yoshida et al. 2003). Halo cores at higher central densities are departing from the approximations used in the above estimate and thus have values of the  $H_2$  fraction that are not quite the equilibrium values. Halo cores which have reached core  $H_2$  fractions higher than  $\sim 10^{-4}$  have been able to cool to significantly below the virial temperature (since the cooling time is much less than the Hubble time at that value of the  $H_2$  fraction), allowing the baryon density to increase. The effect of cooling can also be seen in the plot of radial velocity as a function of radius, where the core regions of halos that have cooled are contracting (albeit very slowly), while those which are still at the virial temperature are not showing significant signs of contraction within  $\sim 20 \text{ pc}$ . All halos have some inflow at large radii, due to the infall of gas from adjoining filaments.

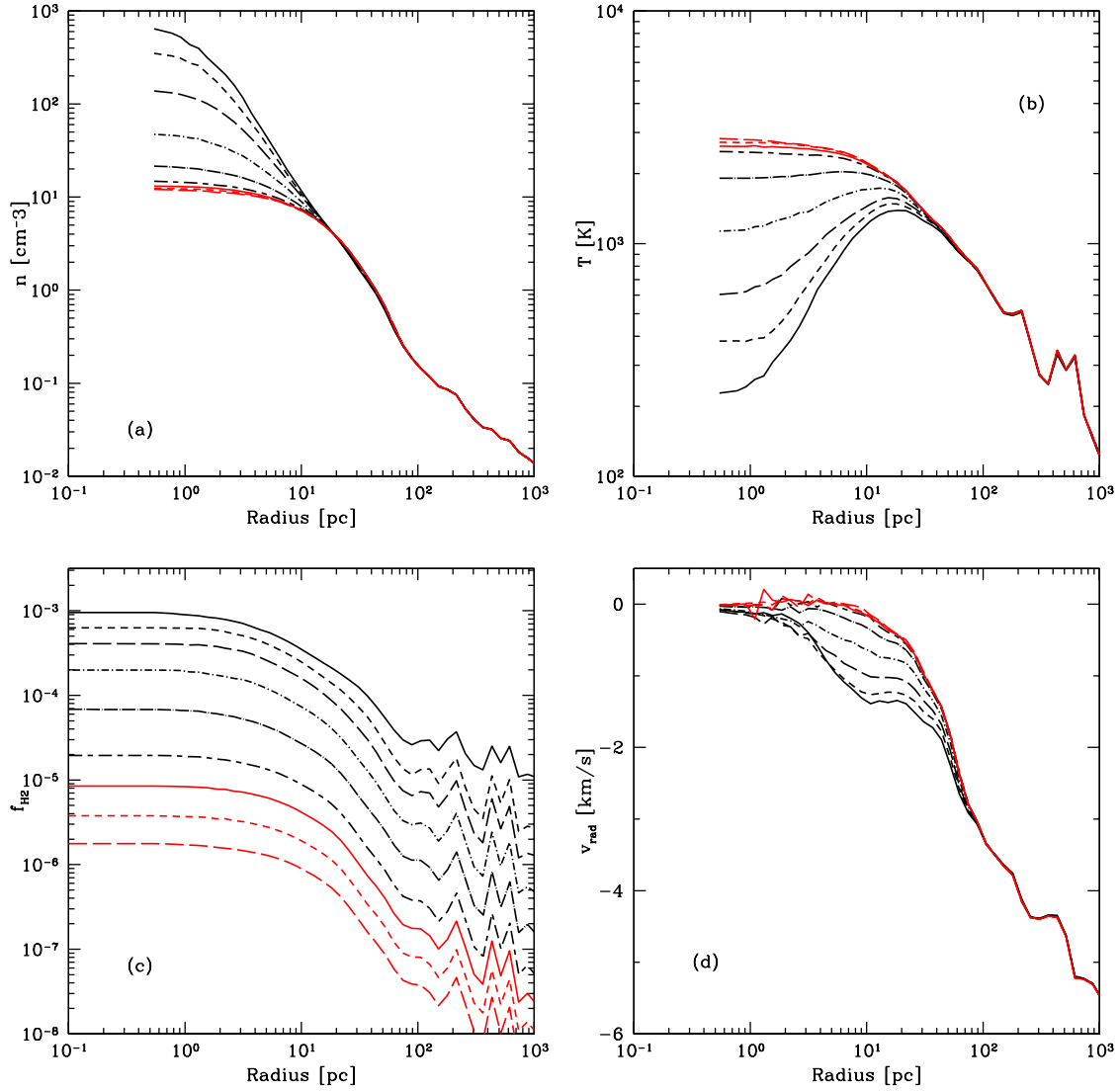


Fig. 12.— Several spherically-averaged baryon quantities for simulations with all values of  $J_{21}$ . Panel (a): Number density as a function of radius. Panel (b): Temperature as a function of radius. Panel (c):  $H_2$  fraction as a function of radius. Panel (d): Radial velocity as a function of radius. All quantities except enclosed gas mass are mass-weighted, and all simulations are shown at  $z = 25$  (shortly before the  $J_{21} = 0$  simulation collapses to high density). Line types and weights correspond to simulations, as follows. Black solid line:  $J_{21} = 0.0$ . Black short-dashed line:  $J_{21} = 10^{-3}$ . Black long-dashed line:  $J_{21} = 10^{-2.5}$ . Black dot short-dashed line:  $J_{21} = 10^{-2}$ . Black dot long-dashed line:  $J_{21} = 10^{-1.5}$ . Black short dashed-long dashed line:  $J_{21} = 10^{-1}$ . Red solid line:  $J_{21} = 10^{-0.67}$ . Red short-dashed line:  $J_{21} = 10^{-0.33}$ . Red long-dashed line:  $J_{21} = 1$ .

## 7. Evolution of two representative halos

In this section we compare the evolution of two representative simulations. We choose the calculations which correspond to  $J_{21} = 0$  and 1. These two simulations represent the extremes in halo evolution – the  $J_{21} = 0$  calculation is an example of the evolution of a “standard” halo, as discussed in previous literature, and the  $J_{21} = 1$  simulation is the most extreme example of a Population III protostar forming in a  $T_{vir} \sim 10^4$  K halo available from our suite of calculations. As described in Section 2.2, both calculations start from the same initial conditions, with only the strength of the LW background being different.

Projections of the log baryon density and temperature for the  $J_{21} = 0$  and 1 simulations are shown in Figures 1 and 2, respectively. These projections are at the epoch of collapse, which is  $z = 24.1$  (17.3) for the  $J_{21} = 0$  (1) simulation. The halo masses are significantly different:  $5.68 \times 10^5$  and  $1.26 \times 10^7 M_\odot$  for the two calculations, reflecting the rapid pace of mergers at that redshift, and the amount of structure evolution that takes place over that relatively short time period ( $\sim 8.2 \times 10^7$  years). This can clearly be seen in the left column of both figures, when the large amount of structure apparent in Figure 1 has merged into the main halo by the time of protostellar cloud formation in the  $J_{21} = 1$  case, as seen in Figure 2.

Despite the differences in evolutionary states, the halos themselves are quite similar in Figures 1 and 2. Both calculations show halos that are strongly centrally concentrated, as shown by the center column in both figures. This column shows projections of the halos which are centered on the baryon peak and are approximately one virial radius across (and thus are scaled differently in both images). No fragmentation of the halo core is visible. The rightmost panel in both calculations shows the center of the halo, where the protostellar cloud is evolving. There is still no evidence for fragmentation up to a central baryon density of  $n \sim 10^{10} \text{ cm}^{-3}$ .

Figures 13 and 14 show the temporal evolution of several spherically-averaged baryon quantities for the  $J_{21} = 0$  and 1 calculations, respectively. These plots show baryon number density, enclosed baryon mass, temperature,  $H_2$  fraction, ratio of cooling time to sound crossing time, and ratio of cooling time to dynamical time, as a function of radius, evolving from a number density of  $\simeq 10 \text{ cm}^{-3}$  to  $\simeq 10^{10} \text{ cm}^{-3}$  in both calculations. Some qualitative commonalities are obvious between the two calculations. Both halos steadily grow in central density (Panel (a)), which is coupled to the growing molecular hydrogen fraction in the central region of the halo (Panel (d)). Both halos collapse quasi-statically, as shown in panels (e) and (f). Also, the temperature profiles (as shown in Panel (c)) are broadly similar, in that the gas in the halo central region cools to some minimum value at  $r \sim 1 - 2$  pc (corresponding to  $n \sim 10^4 \text{ cm}^{-3}$  in both simulations) and then creeps steadily upward as



gas collapses to higher densities.

Though there are qualitative similarities between the evolution of the two calculations, detailed examination shows some significant quantitative differences. The time that the halo in the  $J_{21} = 0$  simulation takes to evolve from a central density of  $n \simeq 10 \text{ cm}^{-3}$  to  $10^{10} \text{ cm}^{-3}$  is  $\simeq 24 \text{ Myr}$ , with 21 Myr of that being the time required to evolve from  $n \simeq 10$  to  $n \simeq 10^4 \text{ cm}^{-3}$ . The time required for the  $J_{21} = 1$  calculation to evolve from  $n \simeq 10 \text{ cm}^{-3}$  to  $10^{10} \text{ cm}^{-3}$  is slightly shorter,  $\simeq 17 \text{ Myrs}$ , with 8 Myrs required to evolve to  $n \simeq 10^4 \text{ cm}^{-3}$ . The temperature evolution is also somewhat different – the  $J_{21} = 0$  simulation has a minimum temperature at  $r \sim 1 \text{ pc}$  of 200 K, with  $n \simeq 10^{4-3}$  and a molecular hydrogen fraction of  $\simeq 10^{-3}$ , and roughly  $1000 M_{\odot}$  of enclosed gas. As the gas within this radius evolves to higher densities, the temperature increases by a factor of a few, peaking at  $T \sim 500 \text{ K}$  at  $n \sim 10^{10} \text{ cm}^{-3}$ , with  $f_{H_2} \simeq 0.02$ . The gas cooling time within  $r \sim 1 \text{ pc}$  in the  $J_{21} = 0$  simulation is always larger than the sound crossing and dynamical times by at least a factor of two, implying a quasistatic gas contraction at all times.

The  $J_{21} = 1$  simulation evolves somewhat differently. The collapsing gas reaches a minimum temperature of  $\sim 800 \text{ K}$  at  $r \sim 2 \text{ pc}$ , with a baryon density of  $\sim 2 \times 10^3 \text{ cm}^{-3}$ , an enclosed gas mass of roughly  $10^4 M_{\odot}$ , and a molecular hydrogen fraction of  $\sim 10^{-5}$ , two orders of magnitude below that in the  $J_{21} = 0$  calculation at the equivalent temperature minimum. The low  $H_2$  fraction is due to the high LW background radiation flux. As the halo evolves to higher densities, the gas temperature and  $H_2$  fraction also creep upwards. The temperature of the gas when the peak reaches roughly  $10^{10} \text{ cm}^{-3}$  is  $\sim 1200 \text{ K}$ , with a  $H_2$  fraction of  $\sim 4 \times 10^{-3}$ . The cooling time at  $r \sim 2 \text{ pc}$  is an order of magnitude higher than the sound crossing or dynamical times, implying an extremely slow contraction of the gas at that radius. As the central density increases, however, the cooling time becomes lower, with  $T_{cool}/T_{dyn} \sim 0.7$  and  $T_{cool}/T_{cross}$  dipping to  $\sim 0.8$  at its minimum, but the latter increasing toward the central density peak to a ratio of  $\sim 10$ . This implies a more rapid contraction of gas in the halo center in the simulation with a higher UV background, despite the lack of molecular hydrogen. It is also worth noticing that the  $J_{21} = 1$  calculation has  $H_2$  fractions at  $n \sim 10^4$  and  $10^8 \text{ cm}^{-3}$  of  $\simeq 2 \times 10^{-5}$  and  $8 \times 10^{-4}$ , respectively, as compared to  $f_{H_2} \simeq 10^{-3}$  and  $2 \times 10^{-3}$  at the same densities in the  $J_{21} = 0$  calculation.

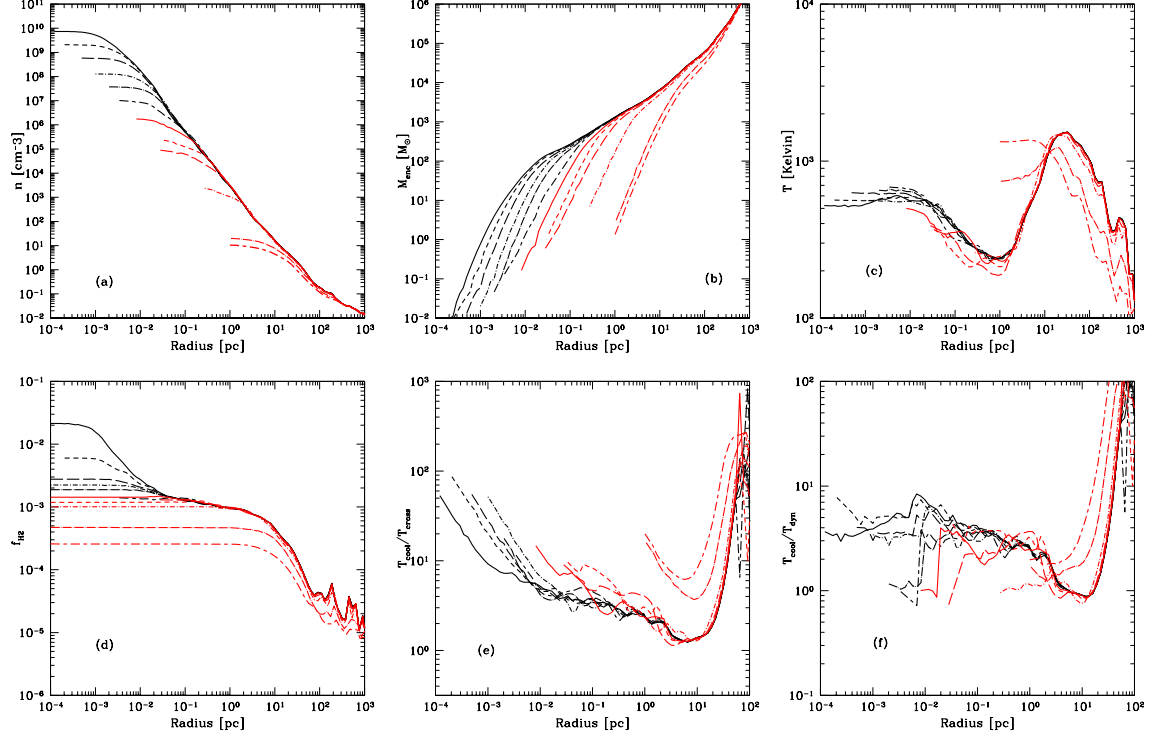


Fig. 13.— Evolution of several spherically-averaged baryon quantities as a function of time for the  $J_{21} = 0$  simulation. Panel (a): Number density as a function of radius. Panel (b): Enclosed gas mass as a function of radius. Panel (c): Temperature as a function of radius. Panel (d):  $H_2$  fraction as a function of radius. Panel (e): Ratio of cooling time to sound crossing time as a function of radius. Panel (f): Ratio of cooling time to dynamical time as a function of radius. All quantities except enclosed gas mass are mass-weighted. Line types and weights correspond to different times, as follows. Red short dashed-long dashed line:  $z = 27.678$ ,  $t = 1.1088 \times 10^8$  years. Red dot long-dashed line:  $z = 26.010$ ,  $\Delta t = 1.0428 \times 10^7$  years. Red dot short-dashed line:  $z = 24.565$ ,  $\Delta t = 1.0428 \times 10^7$  years. Red long-dashed line:  $z = 24.273$ ,  $\Delta t = 2.291 \times 10^6$  years. Red short-dashed line:  $z = 24.171$ ,  $\Delta t = 8.0959 \times 10^5$  years. Red solid line:  $z = 24.148101$ ,  $\Delta t = 1.9034 \times 10^5$  years. Black short dashed-long dashed line:  $z = 24.132556$ ,  $\Delta t = 1.2528 \times 10^5$  years. Black dot long-dashed line:  $z = 24.126839$ ,  $\Delta t = 4.6131 \times 10^4$  years. Black dot short-dashed line:  $z = 24.124178$ ,  $\Delta t = 2.1483 \times 10^4$  years. Black long-dashed line:  $z = 24.121760$ ,  $\Delta t = 1.9517 \times 10^4$  years. Black short-dashed line:  $z = 24.120224$ ,  $\Delta t = 1.2404 \times 10^4$  years. Black solid line:  $z = 24.119543$ ,  $\Delta t = 5.5024 \times 10^3$  years.

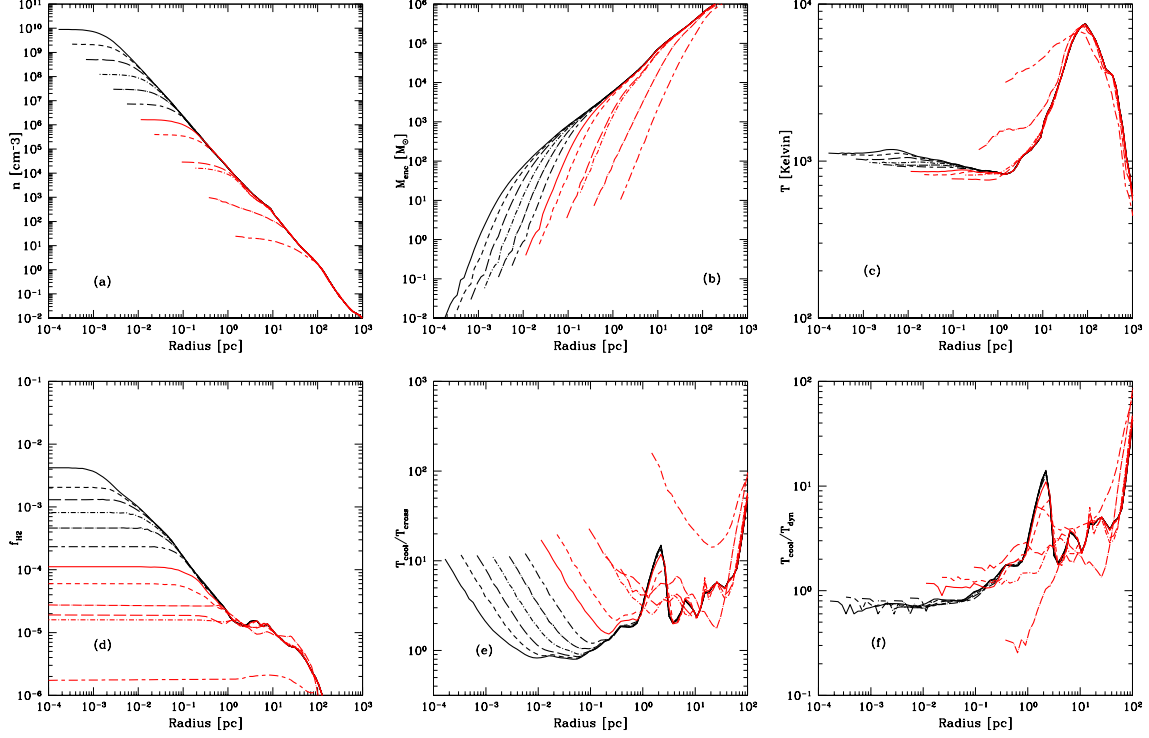


Fig. 14.— Evolution of several spherically-averaged baryon quantities as a function of time for the  $J_{21} = 1$  simulation. Panel (a): Number density as a function of radius. Panel (b): Enclosed gas mass as a function of radius. Panel (c): Temperature as a function of radius. Panel (d):  $H_2$  fraction as a function of radius. Panel (e): Ratio of cooling time to sound crossing time as a function of radius. Panel (f): Ratio of cooling time to dynamical time as a function of radius. All quantities except enclosed gas mass are mass-weighted. Line types and weights correspond to different times, as follows. Red short dashed-long dashed line:  $z = 18.384605$ ,  $t = 1.995 \times 10^8$  years. Red dot long-dashed line:  $z = 17.737221$ ,  $\Delta t = 5.2141 \times 10^6$  years. Red dot short-dashed line:  $z = 17.394373$ ,  $\Delta t = 1.7253 \times 10^6$  years. Red long-dashed line:  $z = 17.373929$ ,  $\Delta t = 3.6030 \times 10^5$  years. Red short-dashed line:  $z = 17.330286$ ,  $\Delta t = 7.7255 \times 10^5$  years. Red solid line:  $z = 17.325077$ ,  $\Delta t = 9.25088 \times 10^4$  years. Black short dashed-long dashed line:  $z = 17.323130$ ,  $\Delta t = 3.4610 \times 10^4$  years. Black dot long-dashed line:  $z = 17.322398$ ,  $\Delta t = 1.3001 \times 10^4$  years. Black dot short-dashed line:  $z = 17.322050$ ,  $\Delta t = 6.1828 \times 10^3$  years. Black long-dashed line:  $z = 17.321880$ ,  $\Delta t = 3.0262 \times 10^3$  years. Black short-dashed line:  $z = 17.321796$ ,  $\Delta t = 1.4813 \times 10^3$  years. Black solid line:  $z = 17.321757$ ,  $\Delta t = 7.0496 \times 10^2$  years.

## 8. Neglected Physics and Possible Numerical issues

In this paper we have examined aspects of the formation of Population III stars in the presence of a soft ultraviolet background, using an adaptive mesh refinement cosmological structure formation code. Given the nature of the tool and current limitations in computing power, some physics were neglected, and possible numerical issues may arise. We discuss this here.

The primordial chemistry model used in these calculations ignores the effects of deuterium, lithium, and the various molecules that form between these elements and ordinary hydrogen. Deuterium and lithium have been shown to be unimportant in the temperature and density regimes that we have examined in this paper (Galli & Palla 1998, 2002; Lipovka, Núñez-López, & Avila-Reese 2005). However, it is possible that they may be relevant in other situations of importance to Population III star formation – in particular, regions which have been ionized to very high electron fractions may experience significant cooling from the HD molecule, which due to its permanent dipole moment makes it more than 100 times more effective as a cooling agent than molecular hydrogen (per molecule), and has the potential to cool gas down to approximately the temperature of the cosmic microwave background, which scales with redshift as  $T_{cmb}(z) = 2.73 \times (1 + z)$  K (Flower et al. 2000; Galli & Palla 2002; Lipovka et al. 2005). This gives a minimum baryon temperature of approximately 55 Kelvin at  $z = 20$  and could reduce the minimum accretion rate onto a primordial protostar significantly. Lithium, while in principle an effective coolant as LiH, is safely ignored, since only a tiny fraction of lithium is converted into LiH (Mizusawa, Omukai, & Nishi 2005). A final chemical process that is omitted from our calculation is heating caused by molecular hydrogen formation at high densities ( $n \gtrsim 10^8 \text{ cm}^{-3}$ ), the inclusion of which may result in differences in the temperature evolution of the gas in the highest density regimes considered here. This does not significantly affect the conclusions of our paper, as the significant differences we observe between simulations occur at densities much lower than  $\sim 10^8 \text{ cm}^{-3}$ .

Self-shielding of the photodissociating background by molecular hydrogen in the high-density gas is ignored in these calculations. Though this effect could in principle be important, the actual column densities of molecular hydrogen are typically far too small to actually block the soft UV flux. According to Machacek et al. (2001) (and references therein), a column density of  $5 \times 10^{14} \text{ cm}^{-2}$  is enough for shielding to become important. However, this was derived for a static distribution of  $\text{H}_2$ , while the LW band consists of hundreds of individual lines whose width in this case is dominated by Doppler broadening. It is useful to note in this case that the average line width is  $\sim 2 \text{ km/s}$  and the RMS baryon velocity in our calculations are  $\sim 4 \text{ km/s}$ . In order for self-shielding to be important in the case of a turbulent medium, the column density must be much higher. Typical maximum  $\text{H}_2$  column densities in our cal-

culations are on the order of  $10^{16} \text{ cm}^{-2}$ , but these occur late in the collapse of the halo core, and in the highest density regions the cooling and  $\text{H}_2$  production times are much shorter than the photodissociation time scale, at which point self-shielding becomes unimportant. It is worth noting that there are some regimes where self-shielding can be critical. Susa (2007) finds that self-shielding can strongly affect the evolution of a collapsing primordial halo which is being illuminated with photodissociating flux by a neighboring star, though the situation is somewhat idealized. Additionally, we do not consider the more complicated effects relating to Population III stars which form in halos in the cosmic neighborhoods where previous generations of stars have existed. This allows us to ignore complex radiative, chemical and dynamical effects that would vastly complicate our calculations (O’Shea et al. 2005a; Johnson, Greif, & Bromm 2006; Yoshida et al. 2006a; Greif et al. 2007; Abel, Wise, & Bryan 2007; Ahn & Shapiro 2007).

A further effect that is ignored in this paper is  $\text{H}^-$  photodetachment. This could in principle be a significant effect –  $\text{H}^-$  is the catalyst for molecular hydrogen formation in the dominant  $\text{H}_2$  formation channel at densities  $\lesssim 10^8 \text{ cm}^{-3}$ , and it can be detached by photons with energies  $h\nu \gtrsim 0.75 \text{ eV}$ . Photons with this energy would be produced in great numbers by the same massive Population III stars that we assume are producing the molecular hydrogen photodissociating background. However, as shown by Machacek et al. (2001), the rate of photodetachment is orders of magnitude smaller than the rate of  $\text{H}^-$  formation at densities comparable to that found in the centers of the halos examined in this work, and thus the process of  $\text{H}^-$  photodetachment can be safely ignored.

In this paper, we examine the effects of molecular hydrogen dissociating backgrounds which range in strength from  $J_{\text{LW}} = 10^{-24}$  to  $10^{-21} \text{ ergs}^{-1} \text{ cm}^{-2} \text{ Hz}^{-1} \text{ sr}^{-1}$  in the LW band (11.18 – 13.6 eV). This range is in good agreement with the expected range of photodissociating backgrounds predicted by Wise & Abel (2005), but it is still finite. Examination of our simulations show that the case with the lowest UV background ( $J_{21} = 10^{-3}$ ) is almost identical to the “control” ( $J_{21} = 0$ ) calculation, justifying our choice of minimum value. Our upper value is consistent with Wise & Abel, and examination of Figures 3 and 9–11 suggests that increases in the strength of the UV background (within reasonable values) will result in a further delay in halo collapse, but no major change in the mode of star formation observed. This is an effect of the halo properties – a small amount of molecular hydrogen will always exist in these halos, allowing the gas at the center to cool and contract quasi-statically to higher densities. Once the gas has collapsed to very high densities, rapid  $\text{H}_2$  formation via the 3-body process will occur, essentially independent of the strength of the soft UV background, and the gas will be able to cool down to  $\simeq 200 \text{ K}$  very quickly.

The effects of magnetic fields are completely ignored in the simulations discussed in this

work. Magnetic fields are discussed in detail in Paper I, but, to summarize, a fairly high seed magnetic field is needed to be dynamically significant at the relatively low densities we explore in this work. The possible importance of magnetic fields has been explored in analytic and semi-analytic work (Tan & McKee 2004; Silk & Langer 2006; Maki & Susa 2007). We will examine the possible evolution of magnetic fields within the context of cosmological AMR simulations in a later paper (O’Shea & Turk 2007, in preparation).

The simulations presented in this paper are generated assuming a cosmology that is somewhat different than the currently-favored WMAP Year III “best-fit” model (Spergel et al. 2006). Most importantly, our value of  $\sigma_8$  is 0.9, which is significantly higher than the WMAP value of 0.761. The general effect of a higher  $\sigma_8$  is to cause structure formation to take place earlier, and thus at a given redshift one would expect significantly more halos in our chosen cosmological model than in the WMAP Year III model. However, the evolution of any single cosmological halo, such as the one examined in this work, is not particularly affected by this parameter in the sense that we are not examining halo statistical properties. In addition to  $\sigma_8$ , the ratio of  $\Omega_b/\Omega_m$  in our simulations is 0.1337, while it is 0.1746 in the WMAP Year III cosmology. This may result in some small quantitative differences in, e.g., the redshift of halo collapse, but should not significantly affect our results.

We direct the reader to Paper I for a detailed discussion of other possible numerical issues, such as the generation of cosmological initial conditions, the assumption that the cold dark matter model is correct, the choice of halo in our simulations, and the size of the simulation volumes used.

## 9. Discussion

This paper explores the formation of Population III stars in simulations with a constant soft UV background. Our results agree well qualitatively with that of Machacek et al. (2001); we both find that a soft UV background can delay the formation of molecular hydrogen, and thus the cooling and collapse, of small ( $\sim 10^6 M_\odot$ ) cosmological halos in which Population III stars form. We also find that increasing the soft UV background increases the minimum halo mass required for a halo to collapse (in a way similar to that of smoothing the dark matter power spectrum at small scales – see O’Shea & Norman (2006) for a discussion). Machacek et al. derived a mass threshold for collapse as a function of the LW background flux that agrees well with our simulations, though the halo masses in our calculation are significantly higher. This is due to the halo that we examine being a “typical” halo rather than at the threshold mass for star formation. Presumably, if we performed these calculations using many halos in a range of cosmological realizations, we would find a minimum halo mass

that is somewhat lower than the masses seen in our calculations. Our work is a significant improvement upon that of Machacek et al. in some respects, as our simulations are much more highly resolved and we examine the evolution of a single halo over a much wider range of soft UV background fluxes. One drawback of our work compared to Machacek et al. is that we examine the evolution of a single halo, albeit with a broad range of UV backgrounds.

Our work is similar to the calculations in Yoshida et al. (2003) which examine Population III star formation in the presence of a photodissociating ultraviolet background. They find that for values of  $J_{LW}$  above  $10^{-23}$  erg s $^{-1}$  cm $^{-2}$  Hz $^{-1}$  sr $^{-1}$ , hydrogen molecules are rapidly dissociated and gas cooling is inefficient, implying that the collapse of gas in the halo center may be delayed until atomic line cooling dominates, in halos with  $T_{vir} \gtrsim 10^4$  K. While we see delays in halo collapse, we do see that a tiny amount of H $_2$  can form even at high FUV background strengths, eventually allowing gas to cool and collapse to high densities without ever reaching temperatures at which atomic line cooling would be effective ( $T \gtrsim 10^4$  K). Yoshida et al. make this statement based on a set of simulations using two different values of  $J_{LW}$  ( $10^{-23}$  and  $10^{-22}$ ), which bracket the “break” in properties seen in our results. The simulations used to obtain this result had SPH particles with  $m_{gas} = 100.0$  h $^{-1}$  M $_{\odot}$  and thus an effective mass resolution comparable to the mass of gas within the quasistatically-collapsing central region of a halo. Our mass resolution is more than two orders of magnitude higher in the center of the cosmological halos that we examine. The differences between our result and theirs is likely due to the significant differences in resolution and may in fact be consistent once resolution is taken into account.

We see a strong relationship between accretion rates onto the protostellar cloud and the strength of the photodissociating background. Calculations with higher ultraviolet background strengths typically have a larger spherically-averaged baryon accretion rate onto the evolving protostellar cloud. This is clearly due to variation in halo central temperature relating to the amount of molecular hydrogen existing in the center of the halo at the epoch of collapse. Accretion onto the evolving protostellar cloud is subsonic, and thus regulated by the local sound speed (which scales as  $T^{0.5}$ ). This implies some relationship between the strength of the photodissociating background and the final stellar mass of the primordial star – however, the details of this relationship are unclear, and depends on many factors. For example, Omukai & Palla (2003) suggest that an increase in accretion rate above  $\dot{m} \simeq 4 \times 10^{-3}$  M $_{\odot}$ /yr will actually result in a *decrease* in the final mass of the star due to radiative feedback from the evolving protostar. However, their results use one-dimensional, fairly idealized models, and geometrical effects may be important. This is explored in Tan & McKee (2004), who use a combination of analytic and semi-analytic models of the evolving system. They suggest that accretion onto the protostar is highly non-spherical, and is in fact mediated by an accretion disk. They argue that a larger accretion rate onto the disk will

lead to a larger star, though with some limitations. Finally, Omukai (2001) and Omukai & Yoshii (2003) study the IMF of stars that form in  $T_{vir} \gtrsim 10^4$  K metal-free protogalaxies in the presence of an  $H_2$  photodissociating background. They conclude that photodissociation actually decreases the Jeans mass of the gas at high densities, and thus reduces the fragmentation mass scale of the clouds and presumably the stellar mass. They use one-dimensional, spherically symmetric simulations, however. We can explore this issue in more detail in later calculations, when appropriate models for shielding, cooling via  $H^-$ , and more advanced chemistry have been implemented into Enzo. This will be examined in a later paper. It is worth noting that the range of accretion rates observed in this situation are within the range of rates seen in the  $\Lambda$ CDM simulations discussed in Paper I. This implies that the mass ranges of the resulting stars will not be significantly different than in the “standard” Population III star formation scenario.

We see no fragmentation of the high-density baryon core, up to a baryon number density of  $n \simeq 10^{10} \text{ cm}^{-3}$ , for the entire range of simulations explored in this paper. This is due to a combination of effects, but predominantly the poor cooling properties of molecular hydrogen. The gas is relatively hot ( $\sim 1000$  Kelvin) and thus has a high sound speed, which helps to damp out perturbations in the halo center which would otherwise result in multiple fragments. This effect is exacerbated in simulations with high ultraviolet background strengths, as the temperatures (and thus the sound speeds) are generally higher. This result implies that there is no fundamental change in the mode of Population III star formation as halos grow, and that more massive “proto-galactic” halos, with  $T_{vir} \gtrsim 10^4$  K, will continue to form a single massive star per halo. These halos will have a much larger binding energy than the smaller,  $M \sim 10^5 - 10^6 M_\odot$  halos which have traditionally been examined by numerical simulations, and implies that multiple generations of star formation may be able to take place in a single halo. This leads to the possibility of “self-enrichment,” where a single Population III star enriches the high-density center of the halo to metallicities high enough to change the cooling properties of the gas. This could cause a strong change in the IMF (Santoro & Shull 2006; Smith & Sigurdsson 2007), and these objects could make a significant contribution to the reionization history of the universe (Mackey, Bromm, & Hernquist 2003; Greif & Bromm 2006). We will examine whether the high-density gas in the centers of these more massive halos fragments in a later work.

The values of accretion rates onto the evolving protostellar cloud which are observed with increasing photodissociating background flux (which are always comparable to those observed in Paper I), in addition to the apparent lack of fragmentation of gas in the halo center up to densities of  $n_h \sim 10^{10} \text{ cm}^{-3}$ , implies that there is no major change in the mass range of Population III stars as halo masses increase to  $T_{vir} \sim 10^4$  K. This is in mild disagreement with previous semianalytic results by Oh & Haiman (2002) and Mackey



et al. (2003). This is apparently because previous authors assumed that  $\text{H}_2$  cooling in “second generation” ( $T_{\text{vir}} \gtrsim 10^4$  K) objects is unimportant, while we observe that a small  $\text{H}_2$  fraction, which forms in equilibrium with the UV background, can cool gas effectively to temperatures of  $\simeq 1000$  K. We do agree with these authors that the majority of primordial star formation will take place in objects with  $T_{\text{vir}} \sim 10^4$  K, the so-called “Second generation” objects (MacIntyre, Santoro, & Thomas 2006)

Our work appears to contradict the results of Greif & Bromm (2006), who use analytic and semianalytic techniques to follow the collapse of gas within halos of  $T_{\text{vir}} > 10^4$ . They find that, in their model, gas cools to  $\sim 8000$  K via atomic line cooling, and then contracts nearly isothermally to high densities, allowing a molecular hydrogen fraction of  $f_{\text{H}_2} \sim 0.001$  to build up independent of local density and temperature. The gas in the center of the halo then cools and allows the gas to fragment on scales of  $\sim 20 M_\odot$ . We do not see this mode of star formation, possibly because we never generate the significantly ionized halos with  $T > 10^4$  K upon which their scenario depends. Rather, we simulate halos that in the cases of  $J_{21} \geq 0.1$  are built up to  $T_{\text{vir}} \sim 10^4$  K via mergers, and the gas is never ionized to a significant degree. One possible reason for the observed differences is that we ignore the formation of deuterium hydride and its effects on the cooling properties of primordial gas. It is possible that, in some contexts, the inclusion of HD may result in enhanced fragmentation. This will be examined in future studies. The scenario described by Oh & Haiman may still in fact be able to occur, and deserves further detailed numerical study to determine the fate of the collapsing gas and the implications of the (presumably) extremely high accretion rates onto the forming protostellar clouds.

Our results are similar to those shown by Wise & Abel (2007), who perform similar simulations examining the collapse of gas in cosmological halos in the presence of a photodissociating background. They also find that, regardless of the strength of the UV background, the collapse of gas in the centers of the cosmological halos in question still occurs via  $\text{H}_2$  cooling. This holds even for quite extreme examples, such as when the original electron fraction is set to unphysically low levels (which should suppress  $\text{H}_2$  formation, at least temporarily).

## 10. Summary

In this paper we have performed a suite of high dynamical range ( $L/\Delta x \sim 5 \times 10^8$ ) 3D adaptive mesh cosmological simulations of the formation of Population III stars in a  $\Lambda$ CDM universe in the presence of a molecular hydrogen photodissociating (“Lyman-Werner”) ultraviolet background. The purpose of these calculations is to understand the effect that the soft ultraviolet background has on the evolution of the gas in collapsing cosmological

halos and to determine possible effects on the forming protostellar cloud. These simulations are all of a single cosmological realization, but with varied ultraviolet background strengths. Our principal results are as follows:

1. Our calculations show that, as the flux of ultraviolet radiation in the Lyman-Werner band is increased, Population III star formation in a given cosmological halo is delayed to later times and, as a result, an increase in the virial mass of this halo at the onset of baryon collapse. This is in good agreement with previous work by Machacek et al. (2001) and Yoshida et al. (2003).

2. We find that, contrary to previous work, the formation of primordial stars is never completely suppressed, regardless of the strength of the UV background. A small amount of molecular hydrogen always exists in cosmological halos, and allows cooling and halo collapse in gas which is bathed in a strong photodissociating background but has not reached  $10^4$  K. The previously-suggested mode of star formation in “second generation” halos, where the collapse of gas to high density is completely suppressed until cooling can take place via atomic hydrogen line transitions, is never observed in our calculations, which have photodissociating background strengths up to  $J_{21} = 1$ .

3. Though the molecular hydrogen fraction in the centers of halos which are bathed in strong ( $J_{21} \geq 0.1$ ) Lyman-Werner radiation is very small at early times ( $f_{H_2} \sim 10^{-6} - 10^{-5}$ ), the gas at the center of the halo can still collapse due to the efficient cooling of molecular hydrogen at  $2 - 5 \times 10^3$  K, and to the extended time these halos require to collapse compared to halos in the presence of much smaller UV backgrounds.

4. We observe that the estimated accretion rate onto the forming protostellar cloud varies strongly as a function of  $J_{LW}$ , with simulations that have a stronger ultraviolet background having higher accretion rates. This is a function of the suppression of molecular hydrogen formation (and thus suppression of effective cooling) by the photodissociating background and of the higher virial temperatures of these halos when the gas finally collapses.

5. Only a single clump is formed at the center of each collapsing cosmological halo, regardless of the strength of the photodissociating background, up to a baryon number density of  $n \sim 10^{10} \text{ cm}^{-3}$ . This implies that, as in the more commonly-studied mode of star formation, we will find only a single star per halo even in objects which are massive enough that  $T_{vir} \gtrsim 10^4$  K.

B.W.O. would like to thank Tom Abel, Greg Bryan, Simon Glover, Thomas Greif, Matthew Turk, and John Wise for useful discussions. This work supported in part by NASA

grant NAG5-12140 and NSF grant AST-0307690. B.W.O. carried out this work under the auspices of the National Nuclear Security Administration of the U.S. Department of Energy at Los Alamos National Laboratory under Contract No. DE-AC52-06NA25396, and was supported by a LANL Director’s Postdoctoral Fellowship (DOE LDRD grant 20051325PRD4). The simulations were performed at SDSC and NCSA with computing time provided by NRAC allocation MCA98N020.

## REFERENCES

- Abel, T., Anninos, P., Zhang, Y., & Norman, M. L. 1997, *New Astronomy*, 2, 181
- Abel, T., Bryan, G. L., & Norman, M. L. 2000, *ApJ*, 540, 39
- . 2002, *Science*, 295, 93
- Abel, T., Wise, J. H., & Bryan, G. L. 2007, *ApJ*, 659, L87
- Ahn, K. & Shapiro, P. R. 2007, *MNRAS*, 375, 881
- Anninos, P., Zhang, Y., Abel, T., & Norman, M. L. 1997, *New Astronomy*, 2, 209
- Berger, M. J. & Colella, P. 1989, *J. Comp. Phys.*, 82, 64
- Bromm, V., Coppi, P. S., & Larson, R. B. 2002, *ApJ*, 564, 23
- Bromm, V. & Loeb, A. 2004, *New Astronomy*, 9, 353
- Bryan, G. & Norman, M. 1997a, 12th Kingston Meeting on Theoretical Astrophysics, proceedings of meeting held in Halifax; Nova Scotia; Canada October 17-19; 1996 (ASP Conference Series # 123), ed. D. Clarke. & M. Fall
- . 1997b, Workshop on Structured Adaptive Mesh Refinement Grid Methods, ed. N. Chrisochoides (IMA Volumes in Mathematics No. 117)
- Bryan, G. L., Norman, M. L., Stone, J. M., Cen, R., & Ostriker, J. P. 1995, *Comp. Phys. Comm*, 89, 149
- Efstathiou, G., Davis, M., White, S. D. M., & Frenk, C. S. 1985, *ApJS*, 57, 241
- Eisenstein, D. J. & Hu, W. 1999, *ApJ*, 511, 5
- Eisenstein, D. J. & Hut, P. 1998, *ApJ*, 498, 137

- Flower, D. R., Le Bourlot, J., Pineau des Forêts, G., & Roueff, E. 2000, *MNRAS*, 314, 753
- Galli, D. & Palla, F. 1998, *A&A*, 335, 403
- . 2002, *Planet. Space Sci.*, 50, 1197
- Gao, L., Yoshida, N., Abel, T., Frenk, C. S., Jenkins, A., & Springel, V. 2006, *ArXiv Astrophysics e-prints*
- Greif, T. H. & Bromm, V. 2006, *MNRAS*, 373, 128
- Greif, T. H., Johnson, J. L., Bromm, V., & Klessen, R. S. 2007, *ArXiv e-prints*, 705
- Hockney, R. W. & Eastwood, J. W. 1988, *Computer Simulation Using Particles* (Institute of Physics Publishing)
- Johnson, J. L., Greif, T. H., & Bromm, V. 2006, *ArXiv Astrophysics e-prints*
- Lipovka, A., Núñez-López, R., & Avila-Reese, V. 2005, *MNRAS*, 361, 850
- Machacek, M. E., Bryan, G. L., & Abel, T. 2001, *ApJ*, 548, 509
- . 2003, *MNRAS*, 338, 273
- MacIntyre, M. A., Santoro, F., & Thomas, P. A. 2006, *MNRAS*, 368, 1301
- Mackey, J., Bromm, V., & Hernquist, L. 2003, *ApJ*, 586, 1
- Maki, H. & Susa, H. 2007, *ArXiv e-prints*, 704
- Mizusawa, H., Omukai, K., & Nishi, R. 2005, *PASJ*, 57, 951
- Norman, M. & Bryan, G. 1999, *Numerical Astrophysics : Proceedings of the International Conference on Numerical Astrophysics 1998 (NAP98)*, held at the National Olympic Memorial Youth Center, Tokyo, Japan, March 10-13, 1998., ed. K. T. S. M. Miyama & T. Hanawa (Kluwer Academic)
- Oh, S. P. & Haiman, Z. 2002, *ApJ*, 569, 558
- Omukai, K. 2001, *ApJ*, 546, 635
- Omukai, K. & Palla, F. 2003, *ApJ*, 589, 677
- Omukai, K. & Yoshii, Y. 2003, *ApJ*, 599, 746

- O’Shea, B., Bryan, G., Bordner, J., Norman, M., Abel, T., & Harkness, R. and Kritsuk, A. 2004, *Adaptive Mesh Refinement - Theory and Applications*, ed. T. Plewa, T. Linde, & G. Weirs (Springer-Verlag)
- O’Shea, B. W., Abel, T., Whalen, D., & Norman, M. L. 2005a, *ApJ*, 628, L5
- O’Shea, B. W., Nagamine, K., Springel, V., Hernquist, L., & Norman, M. L. 2005b, *ApJS*, 160, 1
- O’Shea, B. W. & Norman, M. L. 2006, *ApJ*, 648, 31
- . 2007, *ApJ*, 654, 66
- Peebles, P. J. E. 1968, *ApJ*, 153, 1
- Ripamonti, E. & Abel, T. 2004, *MNRAS*, 348, 1019
- Santoro, F. & Shull, J. M. 2006, *ApJ*, 643, 26
- Scannapieco, E., Madau, P., Woosley, S., Heger, A., & Ferrara, A. 2005, *ApJ*, 633, 1031
- Schaerer, D. 2002, *A&A*, 382, 28
- Schneider, R., Salvaterra, R., Ferrara, A., & Ciardi, B. 2006, *MNRAS*, 369, 825
- Silk, J. & Langer, M. 2006, *MNRAS*, 371, 444
- Smith, B. D. & Sigurdsson, S. 2007, *ApJ*, 661, L5
- Spergel, D. N., Bean, R., Dore, O., Nolte, M. R., Bennett, C. L., Hinshaw, G., Jarosik, N., Komatsu, E., et al. 2006, *ArXiv Astrophysics e-prints*
- Stone, J. M. & Norman, M. L. 1992a, *ApJS*, 80, 753
- . 1992b, *ApJS*, 80, 791
- Susa, H. 2007, *ApJ*, 659, 908
- Tan, J. C. & McKee, C. F. 2004, *ApJ*, 603, 383
- Tegmark, M., Silk, J., Rees, M. J., Blanchard, A., Abel, T., & Palla, F. 1997, *ApJ*, 474, 1
- Truelove, J. K., Klein, R. I., McKee, C. F., Holliman, J. H., Howell, L. H., & Greenough, J. A. 1997, *ApJ*, 489, L179+
- Wise, J. H. & Abel, T. 2005, *ApJ*, 629, 615

- Wise, J. H. & Abel, T. 2007, ArXiv Astrophysics e-prints
- Woodward, P. R. & Colella, P. 1984, J. Comp. Phys., 54, 174
- Yoshida, N., Abel, T., Hernquist, L., & Sugiyama, N. 2003, ApJ, 592, 645
- Yoshida, N., Oh, S. P., Kitayama, T., & Hernquist, L. 2006a, ArXiv Astrophysics e-prints
- Yoshida, N., Omukai, K., Hernquist, L., & Abel, T. 2006b, ApJ, 652, 6